Characterizing Peridotite Xenoliths from Southern Vietnam: Insight into the Underlying Lithospheric Mantle

Kirby Hobbs[1], Lynne J Elkins[1], John Lassiter[2], N Hoang[3], and Caroline M Burberry[4]

[1]University of Nebraska-Lincoln
[2]University of Texas at Austin
[3]Vietnam Institute of Science and Technology
[4]University of Nebraska

July 8, 2023

Table S2. Average trace element compositions (ppm) of clinopyroxene (cpx) and orthopyroxene (opx) in Vietnam xenoliths. Uncertainties expressed as 1s standard deviation.

Cpx Sample	Na	Ca	Ti	Rb	Sr	Y	Zr	Nb	La	Ce	Pr	Nd	Sm	Eu	Gd	Tb	Dy	Ho	Er	Tm	Yb	Lu	Hf	Pb	Th	U	Na STD	Ca STD	Ti STD	Rb STD	Sr STD	Y STD	Zr STD	Nb STD	La STD	Ce STD	Pr STD	Nd STD	Sm STD	Eu STD	Gd STD	Tb STD	Dy
VN-1-2018-21-PL-1	[illegible]	[illegible]	[illegible]	[illegible] *	[illegible]	[illegible]	[illegible]	[illegible]	[illegible]	[illegible]	[illegible]	[illegible]	[illegible]	[illegible]	[illegible]	[illegible]	[illegible]	[illegible]	[illegible]	[illegible]	[illegible]	[illegible]	[illegible]	[illegible]	[illegible]	[illegible]	[illegible]	[illegible]	[illegible]	[illegible]	[illegible]	[illegible]	[illegible]	[illegible]	[illegible]	[illegible]	[illegible]	[illegible]	[illegible]	[illegible]	[illegible]	[illegible]	[illegible]
VN-1-2018-21-PL-2	[illegible]	[illegible]	[illegible]	[illegible]	[illegible]	[illegible]	[illegible]	[illegible]	[illegible]	[illegible]	[illegible]	[illegible]	[illegible]	[illegible]	[illegible]	[illegible]	[illegible]	[illegible]	[illegible]	[illegible]	[illegible]	[illegible]	[illegible]	[illegible]	[illegible]	[illegible]	[illegible]	[illegible]	[illegible]	[illegible]	[illegible]	[illegible]	[illegible]	[illegible]	[illegible]	[illegible]	[illegible]	[illegible]	[illegible]	[illegible]	[illegible]	[illegible]	[illegible]
VN-5-	[illegible]	[illegible]	[illegible]	[illegible]	[illegible]	[illegible]	[illegible]	[illegible]	[illegible]	[illegible]	[illegible]	[illegible]	[illegible]	[illegible]	[illegible]	[illegible]	[illegible]	[illegible]	[illegible]	[illegible]	[illegible]	[illegible]	[illegible]	[illegible]	[illegible]	[illegible]	[illegible]	[illegible]	[illegible]	[illegible]	[illegible]	[illegible]	[illegible]	[illegible]	[illegible]	[illegible]	[illegible]	[illegible]	[illegible]	[illegible]	[illegible]	[illegible]	[illegible]

Table S1: Average major element compositions of core and rim measurements for minerals from Vietnam xenoliths. Uncertainties are 1s standard deviation.

Cpx - Core

Sample	n	Na2O	±	Al2O3	±	Cr2O3	±	FeO	±	CaO	±	MgO	±	SiO2	±	MnO	±	NiO	±	TiO2	±	TOTAL	±	Cr#	Fe#	Mg#
VN-2018-21-PL-1	5	1.43	0.08	5.48	0.46	1.01	0.11	2.31	0.05	21.29	0.25	15.66	0.29	52.85	0.35	0.08	0.01	0.05	0.02	0.21	0.01	100.36	0.21	0.11	0.08	0.92
VN-2018-21-PL-2	4	1.88	0.04	6.66	0.12	0.88	0.03	2.13	0.05	20.11	1.43	14.58	0.35	52.79	0.29	0.08	0.0	0.04	0.01	0.35	0.03	99.40	0.41	0.08	0.08	0.92
VN-2018	5	1.83	0.06	6.68	0.22	0.89	0.04	2.23	0.04	20.61	1.19	15.06	0.13	51.73	0.27	0.08	0.01	0.04	0.0	0.48	0.02	99.64	0.13	0.08	0.08	0.92

Characterizing Peridotite Xenoliths from Southern Vietnam: Insight into the Underlying Lithospheric Mantle

Kirby P Hobbs[1], Lynne J. Elkins[1], John C. Lassiter[2], Nguyen Hoang[3], Caroline M. Burberry[1]

[1] University of Nebraska-Lincoln, Lincoln, NE, USA
[2] Jackson School of Geoscience, University of Texas at Austin, Austin, TX, USA
[3] Institute of Geological Sciences, Vietnam Academy of Science and Technology (VAST), Hanoi, Vietnam

Abstract

We present data for lithospheric mantle xenoliths sampled from two alkali basalts in south-central Vietnam, Pleiku and Xuan Loc, including fertile spinel peridotites. To better determine the origins of the Indochinese subcontinental lithospheric mantle (SCLM), including impacts of posited tectonic extrusion, we present major and trace elements, and $^{87}Sr/^{86}Sr$, $^{143}Nd/^{144}Nd$, $^{176}Hf/^{177}Hf$, $^{206}Pb/^{204}Pb$, $^{207}Pb/^{204}Pb$, and $^{208}Pb/^{204}Pb$ in xenolith mineral separates.

Most peridotites from Pleiku and Xuan Loc have fertile major element compositions, “depleted” and “spoon-shaped” rare earth element (REE) patterns, interpreted to record prior melt depletion followed by melt metasomatism, and variable but generally depleted isotopic signatures (e.g., $^{87}Sr/^{86}Sr$ = 0.70238–0.70337 and $^{143}Nd/^{144}Nd$ = 0.512921–0.514190). A small group of refractory peridotites have “enriched” REE patterns suggesting more extensive metasomatism, and enriched isotope ratios ($^{87}Sr/^{86}Sr$ = 0.70405 and $^{143}Nd/^{144}Nd$ = 0.512755-0.512800). The presence of both fertile and refractory xenoliths records a heterogeneous SCLM beneath Vietnam. Based on geothermobarometry calculations, fertile xenoliths have equilibrium temperatures of 923-1,034 °C and pressures of 11.7-15.8 kbar, while refractory xenoliths have comparable temperatures of 923-1,006 ºC, but lower pressures of 7.1-10.0 kbar, suggesting refractory rocks are dominantly present at shallower depths.

We suggest that the lithospheric mantle has experienced variable melt extraction around 1.0-1.3 Ga, producing heterogeneous major element compositions. While we cannot rule out partial removal and replacement of the lithosphere, large-scale delamination is not necessary to explain observed characteristics. The entire SCLM was more recently metasomatized by melts

resembling Cenozoic basalts, suggesting recent asthenospheric melting has modified the SCLM by melt infiltration.

Key Points

Main point #1: Lithospheric mantle xenoliths in Vietnam record a heterogeneous SCLM beneath Indochina, containing fertile and refractory compositions

Main point #2: Refractory xenoliths overall derive from shallower depths than fertile xenoliths, suggesting a chemically stratified Indochinese SCLM

Main point #3: The SCLM was metasomatized by melts resembling Cenozoic basalts, suggesting only one melt infiltration event that does not require delamination

1. Introduction

The diffuse igneous province of Indochina is a collision-adjacent, complex tectonic region with extensive basaltic magmatism (Hoang & Flower, 1998; Hoang et al., 1996). Vietnamese Cenozoic plateau basalts record two-stage eruptive cycles that initiated ~17 Ma, and consist of large volumes of tholeiitic basalt followed by smaller quantities of alkaline basalt eruptions, several of which host crustal and lithospheric mantle xenoliths (e.g., Anh et al., 2021; Hoang & Flower, 1998; Hoang et al, 1996; Nguyen & Kil, 2019, 2020). Prior geochemical analysis of Vietnamese basalts has included major element and trace element compositions and $^{87}Sr/^{86}Sr$, $^{143}Nd/^{144}Nd$, $^{206}Pb/^{204}Pb$, $^{207}Pb/^{204}Pb$, and $^{208}Pb/^{204}Pb$ isotopes, and suggests that early-stage tholeiitic volcanism may record partial melt contributions from a subcontinental lithospheric mantle (SCLM) source, while later-stage volcanism derives from an asthenospheric source (Hoang & Flower, 1998; Hoang et al., 1996). Hoang et al. (2013) further suggested that some early-stage volcanism may have been moderately chemically contaminated by crustal assimilation. Traditional tectonic regimes associated with mantle upwelling and partial melting, such as regional extension, do not adequately explain the observed abundance (70,000 km^2) of volcanic activity in Indochina (Hoang & Flower, 1998). Previous studies have instead proposed a role for extrusion tectonics, positing that the adjacent Himalayan collision extruded Southeast Asia eastward and caused accompanying local mantle upwelling beneath Indochina (Figure 1) (Flower et al., 1998; Hoang & Flower, 1998; Hoang et al., 1996, 2013; Jolivet et al., 2018). However, the origin and character of the proposed mantle upwelling and associated partial melting have not been clearly explained.

Lithospheric mantle xenoliths provide an opportunity to constrain the depth, temperature, and composition of the local SCLM, and thereby better understand part of the local partial melting and melt transport environment beneath a continent (e.g., Byerly & Lassiter, 2012). Subcontinental lithospheric mantle is typically an ancient, cold layer, variably enriched in trace elements, that separates the continental crust from the underlying convecting asthenosphere (McDonough, 1990). Lithospheric mantle xenoliths are typically thought to represent either the ancient SCLM or, in some circumstances, younger, more recently emplaced asthenosphere beneath continents (e.g., Byerly & Lassiter, 2012; Chu et al., 2009), and may track underlying magmatic processes such as partial melting, melt enrichment, and metasomatic events. For example, major and trace element concentrations in mantle xenolith mineral phases can be used to calculate the equilibration temperature and pressure history of a xenolith, which can in turn be used to infer the thickness and thermal evolution of the SCLM (Ballhaus et al., 1991; Brey & Kohler, 1990; Liang et al., 2013; Lierman & Ganguly, 2003; Putirka, 2008). Mantle xenoliths thus provide a "window" into the SCLM, and by characterizing the SCLM spatially and temporally, we can further constrain local lithospheric and mantle dynamics to inform more realistic tectonic and dynamical models.

To date, mantle xenoliths from Vietnam have not clearly constrained the regional tectonics and dynamics in Indochina. Recent studies in central Vietnam at the Pleiku and Dalat volcanic centers have suggested that the mantle beneath Indochina experienced both a prior melt depletion event and various chemical re-enrichment processes (Anh et al., 2021; Nguyen & Kil, 2019, 2020). Pleiku lithospheric mantle xenoliths from Nguyen and Kil (2019) have estimated two-pyroxene equilibrium temperatures ranging from 825-1131ºC and may have experienced 1-20% fractional melting, followed by silicate melt metasomatism. Xenoliths from locations farther to the south in the Dalat volcanic center, including Ba Ria and Nui Nua, have likewise experienced low degrees of melt extraction (1-13%), equilibrated between 714-1211ºC, and experienced varying degrees of metasomatism (Anh et al., 2021; Nguyen & Kil, 2020). Our current study expands this xenolith dataset and further characterizes the local Vietnamese SCLM using additional major and trace element and $^{87}Sr/^{86}Sr$, $^{143}Nd/^{144}Nd$, $^{176}Hf/^{177}Hf$, $^{206}Pb/^{204}Pb$, $^{207}Pb/^{204}Pb$, and $^{208}Pb/^{204}Pb$ compositions, for additional xenoliths collected from the Pleiku and Xuan Loc (south-central Vietnam) volcanic centers, comprising a total of 25 new spinel peridotite samples (Table 1, Figure 1b). The three objectives of this study are to: (1) track magmatic processes in the local SCLM; (2) compare the SCLM sampled by xenoliths across two different sites in Vietnam, to better characterize its spatial variability (Pleiku and Xuan Loc); and (3) better constrain local mantle evolution beneath a tectonically extruding Indochina.

2. Background

2.1. Geologic Background

Indochina was rifted from Gondwana and subsequently sutured to Asia during the closure of a series of Tethyan ocean basins in the Permian and Triassic (Metcalfe, 2013). Subsequent subduction-related magmatism occurred over Indochina during the Cretaceous as a result of northward subduction of the Tethyan seafloor, emplacing Cordilleran-type granitic batholiths (Gibbons et al., 2015; Shellnutt et al., 2013). The initial collision of Indian continental lithosphere with Eurasia occurred in the Miocene at ~50 Ma (Gibbons et al., 2015). The continued movement of the Indian block northward (~3000 km) after the initial continental collision led to the onset of extrusion tectonics in Asia by 35 Ma (Rohrmann et al., 2012; Royden et al., 2008). The extrusion and clockwise rotation of Indochina occurred as left-lateral movement along large-scale block-bounding, regional transform faults (Figure 1a) (the Ailao Shan-Red River Fault Zone and Mae Ping Fault Zone) from ~35 to ~17 Ma, when motion along the transform faults became right-lateral, coeval with the cessation of South China Sea/East Vietnam Sea rifting (Li et al., 2015; Zhu et al., 2009). This reconfiguration event was accompanied by the onset of diffuse volcanic activity in Indochina at ~17 Ma, which has continued through the Holocene and peaked within the last 3 Ma (Hoang & Flower, 1998; Hoang et al., 1996). The dominant driving mechanism of anomalous Cenozoic basaltic magmatism across Indochina has alternatively been attributed to either ongoing, reorganized extrusion tectonics, or the onset of a new phase of regional continental extension (Cullen et al., 2010; Flower et al., 1998; Hoang & Flower, 1998). The continued extrusional tectonic scenario, accompanied by coupled mantle flow and local upwelling, was suggested as an explanation for the observed local sequences of 1) early-stage tholeiites, proposed to be partial melts of refractory SCLM due to the arrival of extruded, possibly upwelling asthenospheric mantle and associated lithospheric heating, followed by 2) alkali basalts, thought to be partial melts sourced from the decompressing asthenosphere.

The basaltic plateaus across central and southern Vietnam cover an area of 23,000 km^2 and have an estimated volume of ~8,000 km^3 (Hoang & Flower, 1998). The Pleiku basaltic plateau (Figure 1b) covers an area of ~4,000 km^2 and is characterized by the two-stage eruptive cycle typical of most eruptive centers in southern Vietnam (Hoang & Flower, 1998; Hoang et al., 2013). The Xuan Loc plateau basalts cover a smaller area of ~2400 km^2 (Figure 1b) (Hoang et al., 2013). The earlier stage eruptive units at both localities consist of quartz and olivine tholeiites with relatively high SiO_2 (48-55 wt.%) and low FeO (8.0-10.5 wt.%) and have been dated at Pleiku from 6.5-3.4 Ma using $^{40}Ar/^{39}Ar$ methods (Hoang & Flower, 1998; Hoang et al., 1996, 2013). In both locations, a series of tholeiitic flows is overlain by smaller eruptions of predominantly alkali basalt, with relatively low SiO_2 (40-50 wt.%) and high FeO (9.0-14.5 wt.%)

that have been dated at Pleiku from 2.4-0.2 Ma (Hoang & Flower, 1998; Hoang et al., 1996, 2013). Although the individual flows have not been measured in as much detail, Xuan Loc plateau basalts span a similar range of measured ages to the Pleiku lavas (5.0-0.3 Ma) (Hoang et al., 2013).

Alkali basalts from both volcanic plateaus host numerous mantle-derived xenoliths including spinel lherzolites, spinel harzburgites, wehrlites, websterites, and pyroxenites (Hoang & Flower, 1998; Hoang et al., 2013, Nguyen & Kil, 2019, 2020). Basalts from both localities have $^{206}Pb/^{204}Pb$, $^{207}Pb/^{204}Pb$, $^{208}Pb/^{204}Pb$, $^{87}Sr/^{86}Sr$, and ε_{Nd} compositions that extend from the Indian MORB field towards a more enriched composition that resembles the Enriched Mantle 2 (EM2) mantle component (e.g., Sims & Hart, 2006; Workman et al., 2004) (where "enriched" refers to elevated time-integrated incompatible element concentrations recorded as relatively high $^{206}Pb/^{204}Pb$, $^{207}Pb/^{204}Pb$, $^{208}Pb/^{204}Pb$, $^{87}Sr/^{86}Sr$ and low ε_{Nd} and ε_{Hf}), with slightly more enriched isotopic compositions in Pleiku basalts relative to Xuan Loc; tholeiitic basalts likewise exhibit more enriched isotopic compositions overall relative to the alkali basalts (Hoang et al., 1996; 2013).

2.2. Tracking magmatic processes in the SCLM

The compositions of mantle xenoliths provide insight into magmatic processes that have affected the local lithospheric mantle, such as the nature of prior melt extraction (e.g., the degree of melting), which depletes residual peridotites in incompatible elements (Frey & Green, 1974; Michael & Bonatti, 1985). Melting models can help to infer degrees of prior melting, given the measured incompatible element concentrations of the residual rock. To apply these methods to the study of residual rocks, Johnson et al. (1990) revised the basic melting equations of Gast (1968) and Shaw (1970) to describe melting as the change of element concentration in clinopyroxene (cpx) during melting of mantle peridotites, because cpx hosts the highest concentrations of incompatible trace elements.

Metasomatism, the process of fluid (aqueous or carbonitic)-rock or silicate melt-rock reaction, can also affect incompatible element concentrations in lithospheric mantle rocks. Metasomatism is considered "modal" when the metasomatic agent introduces new phases (i.e., precipitates new minerals along reactive pathways) and "cryptic" when reactions are only recorded in trace element compositions (Dawson, 1984). Because metasomatism can partially or fully overprint previous magmatic events, however, simultaneously deciphering the characteristics (e.g., source, timing, and melt/fluid compositions) of both metasomatism and partial melting processes is potentially complex (Ionov, 2002). For instance, the trace element makeup of the metasomatic agent itself is a controlling factor over the resulting trace elements patterns in the host rock. Highly variable and heterogeneous metasomatic enrichment of trace elements in local rocks can likewise be produced by chromatographic fractionation of elements around, e.g., interstitial fluid-filled veins in peridotites; such chromatographic processes may preferentially re-enrich harzburgites over lherzolites in trace elements (Navon & Stolper, 1987; Toramaru & Fujii, 1986). From modelling results, Ionov et al. (2002) suggested that such chromatographic fractionation effects could cause wide ranges of trace element patterns in host rocks during a single metasomatic event, where some rocks develop trace element patterns primarily controlled by the composition of the metasomatic agent, while others are controlled by trace element fractionation between coexisting phases. Despite the described complexity, we can nonetheless interpret the trace element concentrations and radiogenic isotope compositions of lithospheric mantle xenoliths to better understand the magmatic history of the SCLM using a combination of partial melting and temperature and pressure equilibration models, as explored further below.

3. Analytical Methods

3.1. Electron microprobe analysis

The analytical techniques for this study were conducted at the University of Texas at Austin. Major elements for spinel (sp), orthopyroxene (opx), cpx, and olivine (ol) were measured on mineral separates in epoxy mounts with a JEOL JXA-8200 electron microprobe analyzer (EPMA) with wavelength dispersive spectrometry (WDS). Generally, at least one core and rim measurement were analyzed per grain, and typically five grains were measured for each sample. Analytical spot size was a diameter of 2 μm with a beam voltage of 15 kV and an operating current of 50 nA. Elemental concentrations were acquired using Kα peak signals with analyzing crystal detectors, assigned as follows: LiFH – Mn, Ti, Cr; LiF – Fe, Ni; PETH – Ca; TAP – Na, Mg, Al, Si. The on-peak count times were variable for elements in each mineral (40-120 s on-peak, with equal time spent measuring background signals) and correspond to expected element concentrations in a given mineral, with minor elements having longer count times than major elements. The off-peak correction method was linear for all elements in ol and opx (except Ti in ol, for which we used an exponential correction). Spinel was calibrated using the mean atomic number (MAN) background intensity calibration curve. For cpx, we conducted the measurements in two rounds, one using the linear off-peak correction method and the other using the MAN background intensity calibration curve. Natural and synthetic crystalline solids with known major element compositions were used as calibration standards, and the matrix corrections used were ZAF and $\phi(\rho Z)$ (Armstrong, 1988). Average calculated major element concentrations have standard deviations broadly correlated with elemental concentration. Major elements with concentrations > 5 wt.% typically have uncertainties (1σ) < 2% (except for Al), with higher uncertainties ranging from 3-20% in elements with concentrations < 5 wt.%. These uncertainties incorporate both analytical error and intra-sample heterogeneity (Table S1). Such natural heterogeneity within a sample is recorded, for example, in systematic core-rim variations in clinopyroxene Al and Cr content, and in the MgO and FeO variations between grains for sample VN-2018-21-PL-4 (see below).

3.2. In-situ trace element analysis

Trace element measurements were performed for the same cpx and opx epoxy mounts prepared for major element analysis, using an Agilent 7500ce laser-ablation inductively-coupled plasma mass spectrometer (LA-ICP-MS) with a NWR193-FX laser system. The analytical spot size had a diameter of 150 µm, to increase the signal intensity of low trace element concentrations in opx, and overlapped with EPMA spot locations. Samples were pre-ablated, with a dwell time of 60 s and washout time of 30 s. The Si wt.% from the EPMA measurements was used as the internal standard, NIST 612 was used as the primary analytical standard, and NIST 610, BHVO-2G, and NIST 616 were used as secondary standards. Analysis of NIST 610 and BHVO2G for all elements was generally within 5% of accepted values (for NIST 610, [Tm] was < 10 %; for BHVO2G, [Na] and [Nd] were within <10% and [Ca] and [Pb] were <20%). Results of NIST 616 analysis for all elements were within 10 % of expected values, except for elements with concentrations near detection limits (i.e., Nd, Gd, Dy, Ho, and Er, which were within 20 % of expected values). [Ti] and [Yb] for NIST 616, however, did not agree with expected values within 20%. Analyzed NIST 610 concentrations for all measured trace elements are precise within 4% (1σ standard error, with n = 27), with reproducibilities within 6% of expected certified concentrations for all elements, with a mean difference of 2%.

3.3. Sr-Nd-Pb isotope geochemistry

Strontium, Nd, Hf, and Pb isotopes were measured in cpx separates. After hand-picking, the cpx separates were leached using a 2 N HCl solution in an ultrasonic bath for 5 minutes to remove surface coatings. This relatively mild leaching process removes altered rinds and surface coatings from mineral grains, and was only used on the mineral separates analyzed for radiogenic isotopes (that is, not for trace element concentrations, which were all conducted using the *in situ* LA-ICP-MS methods described above). 100 mg of cpx mineral separates from each sample were then dissolved in 5 mL concentrated HF and 1 mL concentrated HNO_3 in an oven at 105°C. After the initial dissolution, samples were dried and then dissolved in 6 N HCl in an oven at 105°C. The samples were redissolved in HCl + HBr and passed through AG1-X8 anion exchange resin to separate Pb. The washes containing Sr and Nd were then dried down and redissolved in HNO_3. The washes were then passed through Sr-Spec resin to separate Sr followed by RE-Spec resin to separate the rare earth elements (REE). Finally, the rare earth portions were converted to a HCl solution and passed through LN-Spec resin to separate Nd from other REE (procedures after Lassiter et al., 2003).

For additional Lu-Hf analysis, handpicked cpx grains were spiked with an enriched ^{176}Lu-^{180}Hf tracer solution and dissolved in a concentrated HF and HNO_3 solution. The separation of Lu and Hf followed procedures outlined in Connelly et al. (2006) and described briefly here. The high field strength elements (HFSE) were separated from a bulk REE fraction using cation exchange chromatography and a dilute HCl + HF solution, and Hf was then separated from other HFSE using TODGA resin in a nitric acid procedure. Bulk REEs were eluted in 6M HCl, and Lu separated from other REEs using TODGA resin and a HNO_3 – dilute HCl procedure.

Lead isotopes were measured using a Nu Plasma 3D multi-collector ICP-MS. Lead separates were diluted to concentrations of 10 ppb in 2% HNO_3 and doped with 2 ppb Tl for pseudo-internal standard normalization. ^{203}Tl and ^{205}Tl were used to correct for mass fractionation of Pb and Hg isotopes using an exponential law. NBS 981 was used for standard-sample-bracketing to correct for analytical drift using the accepted values of $^{206}Pb/^{204}Pb$ = 16.9405, $^{207}Pb/^{204}Pb$ = 15.4967, and $^{208}Pb/^{204}Pb$ = 36.7220. Standard-sample-bracketing was used to linearly interpolate and correct for analytical drift. BCR-2 and BHVO-2 were measured as unknowns to assess external reproducibility; our measured values are largely consistent with values reported by Baker et al. (2004), except for $^{206}Pb/^{204}Pb$ in BHVO-2, where we measured a very minor difference in values from reported compositions (Table 2). Five samples with low Pb concentrations were additionally diluted to a concentration of 0.25 ppb and analyzed using a multi-Daly detector array using sample-standard bracketing with NBS 981 as the bracketing standard (Table 2).

Strontium and Nd isotopes were measured using a Triton thermal ionization mass spectrometer as metals precipitated on Re filaments. We measured NBS 987 $^{87}Sr/^{86}Sr$ = 0.701254 ± 0.000009 (2σ; n=33). BCR-2 and BHVO-2 were measured as unknowns for external reproducibility and are within 0.000008 of accepted values (Table 2). We measured JNdi-1 $^{143}Nd/^{144}Nd$ = 0.512114 ± 0.000013 (2σ; n=15). The cpx mineral separates analyzed generally contained 2.5-50 ng of Pb, 1,000-10,000 ng of Sr, and 100-1,000 ng of Nd, making the impact of procedural blanks (<130 pg Pb; <140 pg Sr; < 200 pg Nd) negligible.

Hafnium and Lu isotopes were diluted and analyzed using the Nu Plasma 3D MC-ICP-MS with a desolvating nebulizer and 100 µL/min aspiration rate. Instrumental mass bias was corrected using the $^{179}Hf/^{177}Hf$ ratio of 0.7325 (Patchett and Tatsumoto, 1980) and then normalized to an in-house Hf isotope standard via sample-standard bracketing. Lutetium was doped with Yb for mass bias corrections, which were conducted using a ratio of $^{173}Yb/^{171}Yb$ = 1.132685, and then were normalized to an in-house Lu standard.

4. Results

4.1. Petrology of Vietnamese mantle xenoliths

Mantle peridotite xenoliths from Pleiku and Xuan Loc are classified as group-1 xenoliths based on the classification scheme by Frey and Prinz (1978) and consist of sp, cpx, opx, and ol (Figure S1). By definition, group-1 xenoliths are typically lherzolites, harzburgites, and dunites that contain Cr-rich, Al_2O_3-poor and TiO_2-poor sp and pyroxenes (Frey & Prinz, 1978). All samples from Pleiku for this study are spinel lherzolites; however, the Pleiku basaltic plateau also contains harzburgite and dunite xenoliths (Hoang et al., 2013; Nguyen & Kil, 2019). Xuan Loc xenolith samples are more diverse, containing lherzolites, harzburgites, and dunites. Sample VN-2018-36-XL-1 is a dunite and only contains ol with minor cpx and sp. Samples have been further subdivided into two groups based on sp Cr# (molar Cr / (Al + Cr)) after methods from Byerly and Lassiter (2012): type-F (fertile) samples have a sp Cr# <0.25 and type-R (refractory) samples have sp Cr# ≥0.25, where the relative "fertility" of the peridotite refers to how readily and productively it can generate magma upon partial melting (Figure 3). Spinel Cr#, as a proxy for peridotite melt fertility, correlates with other indicators of fertility, such as modal cpx, cpx Cr# and Mg#. We further note that for many lithospheric mantle peridotites, peridotite melt fertility is distinct and frequently independent of incompatible element concentrations or radiogenic isotope compositions (e.g., Byerly & Lassiter, 2012); thus, here we differentiate between melt fertility, based on major element compositions, and “enriched” or “depleted” compositions, which we only use to describe trace element and isotopic compositions.

Based on the above sp Cr# definition for fertile and refractory xenoliths, Pleiku samples from this study except for VN-2018-21-PL-4 are all type-F peridotites, while the more southerly Xuan Loc samples contain several samples that are both type-F and type-R peridotites. For comparison, xenoliths from other eruptive centers in the southern Dalat province (including Nui Nua and Ba Ria in the Dalat volcanic plateau) and from Pleiku include both type-R and type-F peridotites (Anh et al., 2021; Nguyen & Kil, 2019, 2020), indicating that both fertile and refractory types have been identified from both sampled regions.

4.2. Major element compositions

Major element data for ol, opx, cpx, and sp mineral separates from Pleiku and Xuan Loc peridotites are provided in Table S1, including both core and rim compositions. Generally, all samples exhibit low heterogeneity on the grain scale between core measurements, except the major element data for sample VN-2018-21-PL-4, which indicate that it is heterogeneous on a grain scale (e.g., FeO and MgO in ol and opx separates of $< 32\%$ and $< 7\%$ RSD, respectively). Clinopyroxene and opx display variations between rim and core measurements in all samples except VN-2018-21-PL-5 and VN-2018-36-XL-11. The core-to-rim variation is present across all localities and sample types (Figure 2). Clinopyroxene Al_2O_3 and Cr_2O_3 concentrations are lower in the rims by ~0.2 to 1.0 wt. % and ~0.1 to 0.2 wt. %, respectively. Similarly, opx grains have rims that are lower by ~0.1 to 0.6 wt. % in Al_2O_3 and by up to 0.1 wt. % in Cr_2O_3. Samples VN-2018-21-PL-1 and VN-2018-36-XL-14 also display rims with slightly higher CaO (0.75 wt.

% and 0.94 wt. %, respectively). In light of this variation, we present average core and rim compositions for each mineral as separate data sets (Table S1).

The Mg# (molar Mg / (Mg + Fe^{2+})) of ol from Pleiku and Xuan Loc xenoliths are between 0.86 and 0.91 (Table S1), which lies within the compositional range of SCLM (Arai, 1994). Lherzolites have overlapping but slightly lower core ol Mg# (0.86-0.91) than harzburgites and dunites (0.89-0.91). Olivine Mg# correlates with cpx Mg#, opx Mg#, and sp Cr#. The CaO content of ol is less than 0.06 wt.% and NiO is between 0.3 to 0.42 wt. % for all samples.

We find that sp compositions are highly variable across Vietnam peridotites. Spinel grains in lherzolites have Al_2O_3 and MgO ranges of 52.9 to 60.0 wt.% and 19.3 to 20.9 wt.%, respectively. Harzburgite and dunite samples have lower Al_2O_3 (32.3-34.6 wt.%) and lower MgO (12.9-16.7 wt.%) than lherzolites. One dunite sample, VN-2018-36-XL-1, has notably higher FeO (26.1 wt.%) and lower Al_2O_3 (24.0 wt.%) than the other refractory, i.e., harzburgite and dunite samples (13.5 wt. % and 33.1 wt. %, respectively). Spinel Cr# for the lherzolites (0.08-0.17) and harzburgites/dunites (0.40-0.50) all lie within the compositional range previously documented for SCLM-derived xenoliths (Arai, 1994).

Lherzolites from Pleiku and Xuan Loc have cpx cores with high Al_2O_3 (5.48-7.37 wt.%), low Cr# (0.06-0.12), and high Na_2O (1.43-1.93 wt.%) (Figure 2b). Clinopyroxene cores from harzburgites generally exhibit comparatively low Al_2O_3 (1.49-2.73 wt.%), high Cr# (0.18-0.38), and low Na_2O (0.57-1.60 wt.%). Orthopyroxene displays a similar pattern to cpx, with lherzolite-hosted grains exhibiting high Al_2O_3 (3.26-4.43 wt.%) and low Cr# (0.04-0.08 wt.%), while opx in harzburgites exhibits relatively low Al_2O_3 (1.86-2.21 wt.%) and high Cr# (0.11-0.16).

4.3. Trace element concentrations

Average trace element data for cpx and opx from Pleiku and Xuan Loc peridotites are provided in Table S2. The primitive mantle normalized trace element concentrations and REE patterns (REE_{PM}) for cpx are shown in Figure 3a-b. Type-F cpx from Pleiku and Xuan Loc display depleted, spoon-shaped, and enriched REE_{PM} patterns. The "depleted" and "spoon-shaped" patterns for Pleiku xenoliths are generally more steeply sloped than those for Xuan Loc samples, with a median $(Ce/Yb)_{PM}$ of 0.17 for Pleiku versus 0.51 for Xuan Loc. Most type-F xenoliths have a relatively flat slope from the middle rare earth elements (MREE) to heavy rare earth elements (HREE), with Pleiku and Xuan Loc having $(Sm/Yb)_{PM}$ from 0.53 to 1.04 and 0.60 to 1.22, respectively. "Depleted" patterns show a positive steep slope from light rare earth elements (LREEs) to MREEs with Pleiku and Xuan Loc showing $(La/Sm)_{PM}$ from 0.10 to 0.14 and 0.33 to 0.61, respectively. "Spoon-shaped" patterns are similar, but also exhibit a LREE enrichment with $(La/Ce)_{PM}$ = 1.08 to 1.79 (Pleiku) and 1.22 and 1.38 (Xuan Loc). VN-2018-36-XL-8 and VN-2018-21-PL-4 have "enriched" REE_{PM} patterns exhibiting negative slopes from LREE to MREE ($(La/Sm)_{PM}$ = 1.55). Similar types of REE patterns have been observed in type-F xenoliths from prior studies in both the Pleiku and Dalat volcanic plateaus (Figure 3) (Anh et al., 2021; Nguyen & Kil, 2019, 2020).

The Type-R cpx have enriched REE_{PM} patterns and, in this study, are only present in the Xuan Loc suite of samples, but similar REE patterns have likewise been reported for published xenolith samples from Dalat and Pleiku (Figure 3a,b) (Anh et al., 2021; Nguyen & Kil, 2019, 2020). Clinopyroxenes from the refractory xenoliths studied here have elevated LREE and low HREE, with steep negative slopes from LREEs to HREEs. These incompatible element enriched patterns exhibit $(Ce/Yb)_{PM}$ from 6.14 to 9.15. Clinopyroxene from sample VN-2018-36-XL-1 has an S-shaped REE_{PM} pattern, with a positive slope from the MREEs to HREEs and $(La/Sm)_{PM}$ of 0.71.

Additional trace element compositions show that other incompatible elements in cpx (Rb, Nb, Pb, Sr, Ti) are overall fractionated compared to the REE (Figure 3c,d). Rubidium in cpx is depleted in almost all samples, with concentrations near or below analytical detection limits. Titanium, Pb, and Nb display negative anomalies across all samples compared to elements with similar incompatibilities in peridotites in Figure 3c-d. Sample VN-2018-21-PL-2 has a steep negative slope from U_{PM} to Pb_{PM}. Strontium is also variably enriched and depleted in the samples when compared to REE_{PM}, and high-Sr samples overall tend to exhibit spoon-shaped REE_{PM} patterns.

Orthopyroxene grains have REE_{PM} concentration patterns that strongly correlate with cpx patterns (Figure 3e). Type-F opx overall have REE_{PM} that exhibit depleted and spoon-shaped patterns. Some opx samples have very low LREE concentrations near analytical detection limits. Type-R opx have convex downward REE_{PM} patterns, with a negative slope from LREE to MREE and a positive slope from MREE to HREE. Moderately incompatible high-field strength elements (HFSE) Ti, Zr, and Hf have positive anomalies relative to REE. The Lu/Hf ratios in opx are also systematically higher by a factor of 3.8 than those in coexisting cpx.

4.4. Radiogenic isotopes

The Sr, Nd, Hf, and Pb isotopic compositions of cpx mineral separates from Pleiku and Xuan Loc are provided in Table 2 and Figure 4. Samples VN-2018-21-PL-1, VN-2018-21-PL-3, VN-2018-21-PL-6, VN-2018-21-PL-7, and VN-2018-21-PL-9 all contained low Pb abundances which necessitated analysis via multi-Daly measurement. Although the analytical uncertainty for these measurements is ~10x greater than for the measurements using Tl for mass fractionation correction (Table 2), these samples fall along the same $^{206}Pb/^{204}Pb$-$^{207}Pb/^{204}Pb$ and $^{206}Pb/^{204}Pb$-$^{208}Pb/^{204}Pb$ correlations as other samples (Figure 4a,c). Clinopyroxenes from Pleiku lherzolites exhibit highly variable isotopic compositions: $^{206}Pb/^{204}Pb$ = 16.69-18.86, $^{207}Pb/^{204}Pb$ = 15.34-15.58, $^{208}Pb/^{204}Pb$ = 36.48–38.85, $^{87}Sr/^{86}Sr$ = 0.70238-0.70337, $^{143}Nd/^{144}Nd$ = 0.513091-0.514190, and $^{176}Hf/^{177}Hf$ = 0.28321–0.28472 (Figure 4). Clinopyroxene grains from the Xuan Loc peridotites display a similar range of isotopic compositions to those from Pleiku: $^{206}Pb/^{204}Pb$ = 17.13-18.37, $^{207}Pb/^{204}Pb$ = 15.44-15.57, $^{208}Pb/^{204}Pb$ = 37.08–38.64, $^{87}Sr/^{86}Sr$ = 0.70257-0.70405, $^{143}Nd/^{144}Nd$ = 0.512755-0.513371, and $^{176}Hf/^{177}Hf$ = 0.28328–0.283809, but the more enriched values (e.g., higher $^{87}Sr/^{86}Sr$ and lower $^{143}Nd/^{144}Nd$) are observed in the refractory samples for that locality.

The cpx Pb isotopic compositions mostly lie near or within the range observed in Indian MORB (Gale et al., 2013) and form positive correlations between $^{206}Pb/^{204}Pb$ and both $^{207}Pb/^{204}Pb$ and $^{208}Pb/^{204}Pb$ that plot above the northern hemisphere reference line (NHRL) (Figure 4a,c). The Xuan Loc cpx compositions also overall exhibit systematically more radiogenic $^{208}Pb/^{204}Pb$ than Pleiku cpx on a plot of $^{208}Pb/^{204}Pb$ versus $^{206}Pb/^{204}Pb$ (Figure 4c). With the exception of one Xuan Loc type-F peridotite, which has more radiogenic ε_{Hf} for a given ε_{Nd} value, all of the measured Vietnam xenoliths (Anh et al., 2021 and this study) exhibit a strong correlation between $^{176}Hf/^{177}Hf$ and $^{143}Nd/^{144}Nd$, similar to most terrestrial rocks (e.g., Vervoort et al., 1999) (Figure 4f).

$^{206}Pb/^{204}Pb$, $^{207}Pb/^{204}Pb$, $^{208}Pb/^{204}Pb$ and $^{87}Sr/^{86}Sr$ in the xenoliths largely do not exhibit well-defined correlations with trace element data, though there is a broad correlation between $^{87}Sr/^{86}Sr$ and Sm/Nd ratios. Clinopyroxene $^{87}Sr/^{86}Sr$ and ε_{Nd} exhibit a negative correlation extending from the Indian-MORB field to highly radiogenic $^{143}Nd/^{144}Nd$ and unradiogenic

$^{87}Sr/^{86}Sr$, most clearly in Pleiku fertile xenoliths (Figure 4d). $^{143}Nd/^{144}Nd$ also exhibits a positive correlation with Sm/Nd ratios and a strong negative correlation with Ce/Yb_{PM} (Figure 5). Type-R xenoliths with $^{87}Sr/^{86}Sr$ and $^{143}Nd/^{144}Nd$ measurements plot at the far right side of the type-F xenolith range, at the enriched limit of the Indian MORB field. Type-F xenoliths also have highly variable $^{143}Nd/^{144}Nd$ (0.512921–0.514190) with many samples plotting to the left of and above the MORB field in Figure 4d; because they are highly correlated, the most radiogenic $^{143}Nd/^{144}Nd$ samples also exhibit highly radiogenic ε_{Hf} (up to +68).

4.5. Thermometry and barometry of Vietnam xenoliths

Calculated equilibrium temperatures and pressures for Vietnam xenoliths from this study are presented in Table 3 and Figure 6. Temperatures based on major element composition were calculated using the two-pyroxene thermometer (T_{BKN}) of Brey and Kohler (1990) and the two-pyroxene thermometer (equation 36) of Putirka (2008) (T_{36}), and temperatures based on REE + Y compositions were calculated using the two-pyroxene thermometer (T_{REE}) of Liang et al. (2013). Averaged core measurements are expected to best preserve the compositions of the peridotites prior to entrainment and exhumation and, thus, have been used here and in the following discussion to characterize the SCLM. The two-pyroxene thermometers used here are predicated on equilibrium between opx and cpx, so it is also important to assess whether any later modification processes (such as metasomatism) have differentially affected the compositions of these two minerals in any samples. A detailed analysis of REE equilibration curves is shown in Figure S2, which illustrates that the HREE are generally in good agreement between cpx and opx in our samples. Figure S3 shows TiO_2 contents for coexisting cpx and opx, and the strong correlation indicates that the minerals are also in equilibrium for major elements.

For T_{BKN}, we assumed a pressure of 15 kbar, and a ±5 kbar change in pressure results in a 10 °C difference in calculated temperature. Temperatures and pressure were also calculated iteratively using equation 36 for temperature (T_{36}) and equation 38 for pressure from Putirka (2008) (P_{38}). The two-pyroxene barometer we used (P_{38}) is temperature-independent. The temperature-dependent barometer of Putirka (2008; equation 39) in principle provides greater precision; however, pressures determined with this barometer were geologically unreasonable, providing either negative values or placing many of the mantle peridotites within the crust (<5 kbar). The pressures calculated using equation P_{38}, in contrast, largely appear geologically reasonable, generally straddling the calculated geotherm estimated from local heat flow (see Section 5.2). Based on our observations and calculated results, the cpx and opx from this study appear to have experienced protracted cooling and subsolidus exsolution. As a result, the cpx and opx compositions have higher and lower wollastonite components, respectively, than the pyroxenes used by Putirka (2008) to calibrate the 2-pyroxene thermobarometers (Putirka, pers. comm.). We thus consider the temperature-independent pressure estimates (P_{38}) to be more accurate for the xenoliths analyzed here.

Equilibration pressures and temperatures of the xenolith samples were determined using the equations described above and by pairing either average cpx and opx core compositions or average cpx and opx rim compositions together, to evaluate multiple possible episodes of equilibration under different conditions. For most samples, core and rim P and T estimates are very similar: the average absolute differences between core and rim temperatures are 10 ºC for T_{36} and 20 ºC for T_{BKN}. Likewise, absolute differences in estimated core and rim pressures average 0.8 kbar, which is well within the ±3.7 kbar uncertainty of the barometer (Putirka, 2008). However, although small on average, differences in estimated core and rim temperatures were systematically larger using T_{BKN} than T_{36}, and several samples had estimated rim temperatures over 50 ºC less than core estimates. In contrast, all rim-core estimated temperatures were within 25 ºC for T_{36} calculations, except for two samples (VN-2018-36-XL-15 and VN-2018-36-XL-19), which had lower estimated rim than core temperatures by differences of 37 and 35 ºC, respectively.

The equilibrium T_{BKN} temperatures for Pleiku and Xuan Loc xenoliths range from 891-1067 ºC and 765-1026 ºC, respectively, calculated using mineral core compositions (Figure 6). Calculated T_{36} values span a narrower range, from 956-1034 and 926-1006 ºC in the Pleiku and Xuan Loc xenoliths, respectively. T_{REE} spans a similar range, with Pleiku xenoliths ranging from 887 to 1032 ºC and Xuan Loc xenoliths from 821 to 1076 ºC. Although on average, T_{REE} and T_{36} are in good agreement (with an average absolute difference of 56 ºC for the full data set), and the differences between the two calculators do not appear to be systematic, several samples have calculated T_{REE} values that are either higher or lower than T_{36} by over 100 ºC. Significantly, both T_{REE} and the absolute difference between T_{REE} and T_{36} are negatively correlated with the calculated pressure, P_{38}. This negative correlation is the opposite of the expected temperature profile for the mantle lithosphere, and we thus consider it to likely be an artifact of the rare earth thermometer inadequately incorporating the pressure dependance of REE partitioning between cpx and opx.

Calculated pressures (P_{38}) for Pleiku xenoliths range from 11.7-15.8 kbar, similar to type-F peridotites from Xuan Loc, which have calculated equilibration pressures of 12.1-16.1 kbar. In contrast, type-R xenoliths have lower pressures ranging from 7.1 to 10.0 kbar. No correlation is observed between P_{38} and the temperatures calculated using the Putirka two-pyroxene thermometer (T_{36}). However, a broad positive correlation between P_{38} and temperature is observed for T_{BKN}. This pressure-temperature correlation roughly parallels the geothermal gradient calculated below (Section 5.2) using the local estimated surface heat flow.

5. Discussion

5.1. Partial melting of the lithospheric mantle beneath Indochina

The observed variations in major element, trace element, and isotopic compositions among Vietnam xenoliths are indicative of mantle residues that have undergone variable degrees of progressive melt extraction and other magmatic processes (e.g., melt addition, refertilization, and metasomatism). The presence of two compositional groups of xenoliths, type-F and type-R, also suggests that the SCLM beneath Indochina may record two distinct histories, although the presence of some overlapping and intermediate compositions among all samples from Vietnam (e.g., Figures 3, 4, and 5) (Anh et al., 2021; Nguyen & Kil, 2019, 2020) makes it less certain that this is the case.

Xenoliths from Pleiku and Xuan Loc span a wide range in composition, from relatively fertile lherzolites characterized by high (>5 wt.%) Al_2O_3 in cpx and low (<0.2) spinel Cr#, to refractory harzburgites with lower Al_2O_3 (<3 wt.%) in cpx and high sp Cr# (>0.4) (Figure 2, 5). Although the additional published data from Anh et al. (2021) and Nguyen and Kil (2019, 2020) include a few intermediate or overlapping compositions, the reported xenolith compositions are largely bimodal, defining fertile (type-F) and refractory (type-R) populations. We interpret these major element variations to primarily indicate that the two populations of xenoliths have experienced different extents of prior partial melting.

Type-R harzburgites and dunites exhibit major element and trace element mineral compositions similar to other mantle xenoliths thought to derive from ancient SCLM (Griffin et al., 2008; McDonough, 1990), namely low Al_2O_3 (1.5-2.8 wt.%), high Mg# (0.918-0.938), and high $(LREE/HREE)_{PM}$ in cpx. Low modal cpx in these samples is also indicative of previous partial melting that consumes clinopyroxene (Herzberg, 1999). Type-R samples from Xuan Loc have high sp Cr#s and strong depletions in HREE (Table S1), which also likely indicate a high degree of partial melt extraction. There is also a strong negative correlation between Ti and sp Cr# across all type-R xenoliths, which can be generated by high degrees of partial melt extraction (Figure 5). The refractory harzburgites from Pleiku (Nguyen & Kil, 2019) also have major and trace element compositions that resemble type-R refractory samples from Xuan Loc, suggesting that both the Pleiku and Xuan Loc volcanic centers overlie SCLM containing highly-depleted residues, while harzburgites from Ba Ria and Nui Nua appear more intermediate, with higher Al_2O_3 that overlaps with the fertile lherzolites from the region (Nguyen & Kil, 2020). Relatedly, refractory xenoliths from Ba Ria and Nui Nua have REE patterns that more closely resemble fertile xenoliths (Nguyen & Kil, 2020), while all type-R xenoliths from both Pleiku and Xuan Loc have relatively high LREE enrichment and are characterized by low ε_{Nd} (+2.3 to +3.2) (Nguyen & Kil, 2019) (Table 2), suggesting an overall complex history of metasomatism or melt-rock interaction.

In contrast, Type-F xenoliths from Vietnam contain cpx with relatively fertile major element compositions (e.g., Al_2O_3 = 5.5 - 7.4 wt.%) that fall within the range of abyssal peridotites, though Vietnamese xenoliths are slightly less fertile than estimates for depleted mantle cpx compositions (~7.9 wt. % Al_2O_3 in cpx) (Warren, 2016; Workman & Hart, 2005). The depleted and spoon-shaped REE_{PM} patterns exhibited by some type-F lherzolites from Pleiku, Xuan Loc, and Dalat are consistent with both partial melting, and modest subsequent enrichment during silicate melt metasomatism (see Section 5.3 for further discussion of metasomatism). Clinopyroxenes from abyssal peridotites display similar LREE patterns to our depleted xenoliths, although they typically exhibit even more extreme LREE depletion (Figure 3) (Warren, 2016, and references therein). While Type-F lherzolites from Pleiku, Xuan Loc, and Dalat all exhibit a range of depleted, spoon-shaped, and LREE-enriched REE_{PM} patterns in cpx, our Pleiku xenoliths are generally more LREE-depleted, extending to lower $(LREE/HREE)_{PM}$ than our Xuan Loc samples (Figure 5) and comparable to the most LREE-depleted Dalat samples from the literature (Anh et al., 2021; Nguyen & Kil 2020). Rather than recording a partial melting history, the trace element depletion patterns in some type-F xenoliths may reflect moderately high degrees of metasomatic enrichment, in agreement with the more radiogenic $^{87}Sr/^{86}Sr$ and unradiogenic ε_{Nd} in many of the fertile xenoliths, and as explored further in Section 5.3. Sample VN-2018-36-XL-8 appears to be the most affected by this character of metasomatic enrichment among the Vietnamese type-F xenoliths: it displays notable LREE-enrichment and has the most enriched radiogenic isotopic composition of the F-type xenoliths analyzed in this study.

Previous studies have shown that sp Cr# and cpx Yb content are well correlated in many mantle peridotites, and can be used to estimate the extent of prior partial melting (e.g., Hellebrand et al., 2001). However, although incompatible trace element abundances and ratios (e.g., La/Sm) should also be strongly affected by partial melting, numerous studies have shown that highly incompatible elements like the LREE are particularly susceptible to subsequent metasomatic reenrichment (e.g., Warren, 2016), and so may not directly record prior melt extraction in lithospheric mantle peridotites. The spoon-shaped and LREE-enriched REE patterns observed in many of the xenoliths examined here thus suggest they have experienced metasomatic enrichment. However, this metasomatism does not appear to have significantly affected either sp compositions or HREE abundances in cpx, as evidenced by the strong correlation between cpx [Yb] and spinel Cr# in our samples (Figure 5).

The melting model of Hellebrand et al. (2001) calculates the degree of fractional melting experienced by mantle peridotites as a function of sp Cr#, assuming an initial LREE-depleted lherzolite composition after Loubet et al. (1975). The Hellebrand et al. (2001) empirical function was derived using melt fractions calculated from Dy, Er, and Yb concentrations, after the approach of Johnson et al. (1990). Calculations using this model for Vietnam xenoliths yield melt fractions of 15-17% for type-R xenoliths from Xuan Loc, and up to 6.1% for type-F xenoliths from both localities (Figure 5). The different xenolith populations are also characterized by notably different pressures of equilibration, with the refractory xenoliths constrained to shallower pressures overall. Our Xuan Loc type-R xenoliths all have pressures < 10 kbar, and type-R xenoliths from the nearby Dalat volcanic plateau have calculated pressure estimates of 9.3 to 12.4 kbar (Nguyn & Kil, 2020). Applying this melting model to the published Pleiku dataset from Nguyen and Kil (2019) yields melt fractions of 10.3-18.5% and up to 7.1% for type-R and type-F xenoliths, respectively, ranges which overlap with or approach results for our samples. However, unlike Xuan Loc xenoliths, the refractory Pleiku xenoliths are not entirely restricted to low (< 10 kbar) equilibration pressures. Nguyen and Kil (2020) likewise estimated partial melting of 1-13% for their harzburgite and lherzolite xenolith samples, and Anh et al. (2021) calculated that their type-F lherzolite xenoliths from Dalat experienced up to 5% partial melting, consistent with our type-F samples.

The major element, trace element, and isotopic variations discussed above thus suggest that the Pleiku and Xuan Loc xenoliths have experienced similar histories of variable melt depletion followed by metasomatism, with the most refractory, melt-depleted harzburgites recording the greatest effects of metasomatism. The timing of these two events is more difficult to constrain, but observed correlations between radiogenic isotopes, especially Hf- and Nd-isotopes, and incompatible elements provide broad constraints.

The Sm/Nd-$^{143}Nd/^{144}Nd$ correlation shown in Figure 5e could be interpreted as a rough isochron, reflecting radiogenic ingrowth since metasomatic processes produced variable LREE enrichment that lowered Sm/Nd ratios. The slope of the correlation in this case would suggest a rough "age" of ~600 Ma. This can be viewed as a maximum age for metasomatism – any younger mixing could generate a similar trend, so the true age could be zero. In fact, most xenoliths fall along a strong correlation between 1/[Nd] and $^{143}Nd/^{144}Nd$ (Figure 7a). Hf-isotopes similarly correlate strongly with inverse Hf concentration (Figure 7b). These linear correlations between inverse concentration and isotopic composition are predicted for two-component mixing. As noted above, the "enriched" end of this mixing array and the most heavily metasomatized xenoliths plot within the $^{87}Sr/^{86}Sr$-$^{143}Nd/^{144}Nd$-$^{206}Pb/^{204}Pb$ field defined by Cenozoic Vietnamese basalts. Thus, a reasonable metasomatizing agent would be the Cenozoic basalts or related melts percolating through the SCLM immediately prior to or concurrent with the magma ascent that brought the xenoliths to the surface, which would indicate a young (<18 Ma; e.g., Hoang and Flower, 1998) age for the metasomatism.

Although most xenoliths have been variably affected by metasomatic overprinting, a small number of fertile xenoliths from Pleiku are characterized by LREE depletion and Sm/Nd and Lu/Hf ratios that extend to higher values than estimates for DMM (Workmann & Hart, 2005). These same xenoliths have $^{143}Nd/^{144}Nd$ and $^{176}Hf/^{177}Hf$ values that extend above what is observed in MORB, requiring a period of radiogenic ingrowth of ^{143}Nd and ^{176}Hf. Given that these samples are the least affected by recent metasomatism, their parent/daughter ratios most closely approach those produced by earlier melt depletion. We therefore calculate DMM-extraction ages for these samples base on the Sm-Nd and Lu-Hf compositions. The four fertile Pleiku samples with $^{143}Nd/^{144}Nd$ values in excess of MORB have model DMM-extraction ages ranging from ~0.7 to 1.3 Ga (Figure 7c). One of these samples, VN-2018-21-PL-2, also has very radiogenic $^{176}Hf/^{177}Hf$ and nearly identical DMM-extraction age estimates based on Sm-Nd (1.13 Ga) and Lu-Hf (1.10 Ga). These melt depletion ages should be treated with caution, as they do not account for inherent heterogeneity in the convecting upper mantle. They also do not allow us to determine whether the melt depletion occurred in association with initial stabilization of the SCLM or within the convecting mantle – similar ultra-depleted isotopic signatures have been found in abyssal peridotites as well as MORB and are increasingly recognized to be present in the convecting upper mantle (Stracke et al., 2011; Sanfilippo et al., 2021). We note, however, that the clustering of model depletion ages around 1 Ga is similar to peak T_{DM} ages determined from Hf-isotopes in several suites of granitic zircons from central and southern Vietnam (Hieu et al., 2016, 2022), suggesting the melt depletion may be related to initial SCLM and crust formation.

5.2. Thermal and chemical structure of the SCLM beneath Pleiku and Xuan Loc

Our pressure and temperature estimates for the Pleiku and Xuan Loc xenoliths, combined with their chemical and isotopic compositions, provide a more detailed picture of the thermal and chemical structure of the SCLM beneath these regions. Figure 8 shows the estimated pressures and temperatures of the Xuan Loc and Pleiku xenoliths for our temperature estimates, using both the Brey & Kohler (1990) two-pyroxene thermometer (T_{BKN}) (Figure 8a) and the two-pyroxene thermometer of Putirka (2008) (T_{36}) (Figure 8b). Using the same methods, we also determined pressure and temperature estimates for the Dalat and Pleiku xenoliths analyzed by Nguyen and

Kil (2019, 2020) and Anh et al. (2021), and these estimates are included in Figure 8 for comparison.

Figure 8 indicates that the calculated xenolith equilibration pressures and temperatures generally cluster near geothermal gradients calculated using regional heat flow data, suggesting they are broadly in agreement with those estimated gradients. Unfortunately, there are currently no local heat flow data in the immediate vicinity of the study area, so best estimates come from regional datasets, which have been compiled into a heat flow map (Hall, 2002). From this map, the estimated heat flow values for our study areas are 85 mW/m^2 and 90 mW/m^2 for Pleiku and Xuan Loc, respectively. The measured thickness of the crust is 32 km at Pleiku and 28 km at Xuan Loc, from broadband seismic data (Yu et al., 2017a). We assumed average densities (ρ) of 2800 kg/m^3 and 3250 kg/m^3 for the crust and mantle, respectively, with thermal conductivities of 2.7 W/(m·K) for the crust and 4.0 W/(m·K) for the mantle (Turcotte & Schubert, 2002). The heat generation *(HG)* of the crust was then calculated using the model of Hasterok and Chapman (2011):

$$HG = 10^{-5}\rho\left[3.5\mathrm{C}_{\mathrm{K_2O}} + 9.67\mathrm{C}_{\mathrm{U}} + 2.63\mathrm{C}_{\mathrm{Th}}\right]$$

where HG is expressed in units of $\mu W/m^3$, and C_i values indicate concentrations for each species i. Here we used the estimated abundances of heat-producing elements in the average continental crust from Rudnick and Fountain (1995): 1.88 w.t% K_2, 5.6 ppm Th, and 1.4 ppm U.

Xenolith P-T estimates using T_{36} are located above and below the estimated geothermal gradients and show no clear correlation between depth and temperature (Figure 8b). In contrast, the P-T estimates using T_{BKN} are generally closer to the geothermal gradients, though shifted to moderately lower temperatures at a given pressure, especially at higher pressures (Figure 8a). One possible explanation for this mismatch is that regional surface heat flow does not reflect a semi-steady-state conductive gradient, but may have been elevated due to heat deposition in the crust during magma transport and storage. Thus, the actual conductive heat flow within the local SCLM may be lower than required to support a measured surface heat flow of 85-90 mW/m^2.

Regardless of the thermometer used, the Dalat and Xuan Loc xenoliths record a chemically stratified lithospheric mantle. Specifically, the population of refractory (type-R) xenoliths from Dalat and Xuan Loc generally have lower estimated pressures than fertile-type xenoliths from Dalat, Xuan Loc, or Pleiku, though the populations do overlap (Figure 8). However, similar stratification is not as clear for the type-R xenoliths sampled at Pleiku, which is located to the north of Dalat and Xuan Loc: although the current study only retrieved fertile (type-F) xenoliths from Pleiku, data from Nguyen and Kil (2019) include type-R Pleiku xenoliths that are not as restricted to shallow equilibration depths. That said, although Pleiku xenoliths do exhibit more overlap, they nonetheless appear to have some depth dependence. For example, in Figure 8, 5-6 Pleiku samples with shallower equilibration depths (< 40 km) are refractory, while the majority of those with greater equilibration pressures are fertile.

The shallower, type-R Xuan Loc xenoliths are also LREE-enriched with relatively unradiogenic $^{143}Nd/^{144}Nd$ signatures compared to the deeper, type-F xenoliths. Figure 8c shows the resulting variations in $^{143}Nd/^{144}Nd$ with estimated depth. Although two type-F Dalat samples have somewhat shallower equilibration pressures relative to their $^{143}Nd/^{144}Nd$ compositions (Anh et al., 2021; Nguyen & Kil, 2020), the other samples record a broad compositional correlation with depth. Correlations between depth and isotopic compositions are weaker for $^{87}Sr/^{86}Sr$ and absent for Pb-isotopes, however, perhaps reflecting a greater sensitivity of Sr and Pb to metasomatic overprinting than Nd in the local lithospheric mantle, whether because of the initial composition of the unmetasomatized type-R peridotites or due to the composition of the metasomatizing fluid, which is explored in further detail in Section 5.3. Although these isotopes may reflect a more complex history, at Xuan Loc and Dalat, the refractory-type lithosphere does appear to be underlain by more fertile, LREE-depleted mantle. One possible explanation for the apparent depth-dependent compositional distribution in Figure 8c, which is consistent with the presence of two largely distinct xenolith populations, is that the refractory samples represent fragments of the original lithospheric mantle, which has since been partially replaced by more fertile material, an interpretation that is consistent with the model suggested by Anh et al. (2021). These more fertile peridotites, in turn, may have been emplaced more recently in a younger, deeper layer, and were derived from the more recently convecting asthenospheric mantle. However, in contrast, both the handful of more intermediate xenolith compositions (e.g., harzburgites with elevated Al_2O_3 and sp Cr# = ~0.25; Nguyen & Kil, 2020), and the correlations shown in Figure 5 suggest that the xenoliths were all affected by a single metasomatic episode or event, which would not necessitate the proposed history of thinning and replacement of the deep lithospheric mantle layer.

The following section explores the metasomatic histories recorded by F- and R-type xenoliths further, and aims to clarify which genetic models are most consistent with all of the observed geochemical correlations and variations in mantle composition with depth.

5.3. Metasomatism of the SCLM beneath Vietnam

Given that LREE are highly incompatible, they should be strongly depleted by removal from the source rock during partial melting. As discussed above, the apparent enrichment in these elements in both fertile and refractory xenoliths with "spoon-shaped" and LREE-enriched REE_{PM} patterns requires an additional explanation, and likely indicates metasomatism of incompatible-element depleted residues by the later addition of a LREE-enriched melt or fluid.

This evidence for variable metasomatic enrichment in all sampled regions (Pleiku, Dalat, and Xuan Loc) raises several related questions: 1) Do the different enrichment patterns observed in the fertile and refractory xenoliths reflect two distinct metasomatic episodes, or are they related to a single event? 2) When did metasomatic enrichment occur? and 3) What was the nature of the metasomatic agent(s)?

One scenario that could explain the character of type-F xenoliths is more recent emplacement of fertile (type-F), young lithospheric mantle from the convecting asthenosphere, similar to the lithospheric replacement model suggested by, e.g., Anh et al. (2021). As discussed previously, refractory xenoliths at Xuan Loc and Dalat are restricted to relatively shallow equilibration pressures ($\leq$ 12.4 kbar; Figure 8). In this scenario, the type-F xenoliths from Pleiku and from the deeper portions of the Xuan Loc and Dalat lithosphere derived from convecting asthenospheric mantle material that was relatively recently emplaced as younger lithosphere, beneath the older refractory rocks. This model is similar to that proposed to explain the presence of a bimodal xenolith population with similar refractory/LREE-enriched and fertile/LREE-depleted characteristics within the Rio Grande Rift, North America (Byerly and Lassiter, 2012) and was previously proposed by Nguyen and Kil (2019) to explain the presence of both refractory and fertile mantle beneath Pleiku. In this scenario, the metasomatic enrichment of the older, refractory xenoliths could reflect addition of subduction-derived melts or fluids during the Mesozoic. The modest metasomatic enrichment observed in some fertile xenoliths with spoon-shaped REE profiles then perhaps reflect a second metasomatic episode, unrelated to that observed in the older refractory xenoliths; this second event could have occurred either before (i.e., still within the convecting asthenosphere) or after emplacement as new lithosphere. In either case, this second metasomatic episode could potentially indicate the addition of low-degree melts generated during tectonic extrusion or otherwise related to Cenozoic volcanism in Vietnam. A third scenario, namely that the refractory lithosphere was already melt-depleted prior to emplacement from asthenosphere, is difficult to completely rule out, but is also not necessary to explain the data.

However, the Pleiku and Xuan Loc xenoliths also display a strong correlation between $^{143}Nd/^{144}Nd$ and LREE enrichment, which strongly suggests a single mixing trend has affected both the refractory and fertile xenoliths. Figure 5 illustrates the correlations between $^{143}Nd/^{144}Nd$ and both Sm/Nd and Ce/Yb, across both (fertile and refractory) xenolith populations, suggesting modification by a single metasomatic agent for all of the xenoliths. Other geochemical patterns (e.g., Figures 3-4) show overlap and intermediate compositions between the xenolith types and locales, shedding doubt on the proposed bimodal character of the SCLM. As a second, alternative scenario, type-F xenoliths in Vietnam may thus record a related but less extensive history of melt-rock interactions to the type-R xenoliths, which would be consistent with the generally lower, and thus more easily modified trace element abundances in the refractory samples. That said, while type-F xenoliths from Pleiku and Xuan Loc share similar characteristics that suggest comparable processes have produced parts of the fertile SCLM in both locations, samples from the two sites do exhibit a noteworthy difference in their trace element and radiogenic isotope compositions, specifically less radiogenic $^{208}Pb/^{204}Pb$ in Pleiku type-F xenoliths compared to those from Xuan Loc. This suggests a slightly different geochemical character to the metasomatic enrichment beneath Pleiku. Nonetheless, the fact that the Xuan Loc and Pleiku fertile xenoliths both fall along the same Ce/Yb-$^{143}Nd/^{144}Nd$ and Sm/Nd-$^{143}Nd/^{144}Nd$ trends, which also extend to the refractory xenolith compositions, strongly suggests that the metasomatism of the fertile and refractory xenoliths occurred as a single event.

In our proposed scenario, this single metasomatic event could be related to modification of the SCLM by subduction-related melts or fluids in the Mesozoic, or it could reflect more recent modification, possibly related to Cenozoic volcanism. A better understanding of the nature of the metasomatic agent(s) (e.g., whether or not the agent is subduction-related) may help to clarify the relationships between mantle lithospheric metasomatism and the tectonic evolution of the regional Indochinese SCLM. Nguyen and Kil (2019) previously suggested that the trace element characteristics of metasomatized, refractory Pleiku xenoliths suggest involvement of a subduction-related carbonate-rich melt and/or H_2O-CO_2-rich fluids, and Anh et al. (2021) similarly advocated for a hydrous silicate metasomatizing agent beneath Dalat. Depletions of Ti relative to HREE and comparative enrichments in LREE in mantle rocks have previously been invoked to characterize the metasomatic agents responsible for melt-rock interactions (Coltorti et al., 1999). Given the notably low Ti/Eu (<1500) and high $(La/Yb)_N$ in type-R cpx from Xuan Loc, such CO_2-rich silicate melts (i.e., subduction-related melts) may be a plausible metasomatic agent here as well. Given the presence of Mesozoic subduction-related granitic batholiths throughout Indochina (Shellnutt et al., 2013; Gibbons et al., 2015), a carbonated silicate melt would also likely support a Mesozoic origin for the metasomatism recorded in the refractory xenoliths.

Subduction-derived, CO_2-rich silicate melts, like those posited to have metasomatized the Pleiku xenoliths (Nguyen and Kil, 2019), are also expected to be enriched in large-ion lithophile elements (e.g., Rb, Sr) and depleted in high field-strength elements (HFSE) like Nb, Zr, and Hf (Ionov, 2002). At first glance, Vietnam xenolith cpx trace element patterns do appear consistent with involvement of a subduction-related, either carbonated or hydrous silicate melt (e.g., Anh et al., 2021), since many samples display depletions in Zr, Hf, and Ti (Figure 3). However, in most samples, these depletions in cpx are mirrored by positive anomalies in the same elements in coexisting opx (Figure 3e). Trace element patterns in cpx are controlled not only by the compositions of melts or fluids added to or removed from the host peridotite, but also by cpx/opx partitioning within the rock, which is a function of mineral composition, temperature, and pressure. Previous studies have demonstrated that HFSE anomalies in peridotitic cpx do not necessarily always reflect HFSE depletion of the bulk peridotite rock, and thus may not uniquely fingerprint a subduction origin for metasomatic enrichment (e.g., Byerly and Lassiter, 2015).

Although the trace element patterns described above provide somewhat ambiguous constraints on the origins of metasomatic overprinting, the isotopic compositions of the refractory and fertile xenoliths suggest the recorded metasomatism may be instead best explained by infiltration of melts similar to Cenozoic Vietnamese volcanic products. The refractory Xuan Loc xenoliths, which appear to record the greatest extent of metasomatic overprinting, have radiogenic isotope compositions that overlap with the depleted end of the field defined by Cenozoic basalts from south and central Vietnam (Figure 4, and references therein). Many of the fertile samples from Xuan Loc, Dalat, and Pleiku, in contrast, overlap with the field defined by Indian MORB, and extend to even more depleted compositions, particularly for Pb and Nd isotopes (Anh et al., 2021; Nguyen & Kil 2019, 2020). Although previous studies have proposed that the local SCLM is a significant melt source component in Cenozoic Vietnamese basalts (Hoang & Flower, 1998; Hoang et al., 1996; Tu et al., 1991, 1992), here we present an alternative interpretation from our xenolith measurements. Because the xenolith population overlaps with Cenozoic basalts in composition (Figure 4), and Figure 7 shows that the Nd and Hf trace element and isotopic compositions are best explained by a mixing trajectory, we posit that recent local basalts, initially generated from enriched, possibly subduction-modified asthenospheric mantle components upwelling beneath the Vietnamese lithosphere, have themselves metasomatized and enriched the local SCLM, and that the refractory lithospheric harzburgites were particularly susceptible to this overprinting.

In summary, although we cannot definitively preclude a scenario in which the refractory and fertile xenolith groups each experienced temporally separate metasomatic events with distinct origins, a more parsimonious interpretation of the correlations observed in Figure 5 is that both suites of xenoliths experienced a single metasomatic event, but were affected to differing degrees; and that this metasomatism is likely related to the same episode of mantle melting that generated the basalts which ultimately brought these xenoliths to the surface.

5.4. Working model of the evolution of SCLM beneath Vietnam

In the analysis above, we have made two potentially conflicting observations: 1) lithospheric mantle xenoliths from Vietnam mostly fall into two distinct populations (type-F and type-R) that have, on average, equilibrated at different depths and experienced different histories of melt extraction, and 2) the mantle xenoliths from Vietnam also exhibit trace element vs. radiogenic isotope compositions that suggest simultaneous metasomatism throughout the regional lithospheric mantle. Both of these observations appear robust: although they overlap, the type-F mantle xenoliths mostly have asthenosphere-like compositions, mineral compositions corresponding to equilibration depths between ~30-55 km (Figure 8), and a limited overall extent of metasomatism compared to type-R xenoliths. Likewise, all measured Vietnamese mantle xenoliths exhibit $^{143}Nd/^{144}Nd$ vs. incompatible element correlations most consistent with a single, partially-overprinting metasomatic event.

Previous studies (e.g., Pan et al., 2013) have suggested that at some time in the past, some portions of the SCLM beneath Vietnam were replaced by asthenospheric mantle. In at least some locations, we also do observe that type-R xenoliths are restricted to shallower areas, suggesting they could derive from older refractory lithosphere that was not replaced. Our depth observations thus suggest that some portions of the older continental lithospheric mantle may have been partially removed by thinning or erosion during a prior event. Even neglecting our calculated mantle temperatures and xenolith trace element compositions, we do note that the xenolith equilibration pressures alone support a relatively thin continental lithospheric layer. The type-F xenoliths likewise exhibit $^{87}Sr/^{86}Sr$ (0.703724-0.703365), ε_{Nd} (+5.51 to +30.28), and ε_{Hf} (+14.9 to +68.5) that range from values resembling ultra-depleted mantle (Byerly and Lassiter, 2014; Cipriani et al., 2011; Mallick et al., 2014; Stracke et al., 2011) to those of MORB (Hofmann, 2007; Salters and Stracke, 2004; Workman and Hart, 2005). Type-F xenoliths also have relatively fertile major element compositions that likely experienced relatively small degrees of prior partial melting, suggesting the xenoliths were previously a part of a moderately depleted mantle region that underwent limited decompression melting.

Determining the pre-metasomatic origins of type-R xenoliths is more complex, given the high levels of overprinting of trace elements and isotopic compositions due to likely more thorough metasomatism (e.g., Figure 3). Mantle xenoliths with similar trace element and isotopic characteristics to the Vietnam type-R xenoliths have previously been attributed, but are not unique to pre-Phanerozoic lithosphere (e.g., Rio Grande Rift, Colorado Plateau, Zealandia, North China Craton, Central Asian Orogenic Belt) (Byerly and Lassiter, 2012; Liu et al., 2012; McDonough, 1990; Pan et al., 2013; Scott et al., 2014; Warren, 2016). Type-R xenoliths from Vietnam (Nguyen and Kil, 2019, 2020) also exhibit some characteristics of peridotites that have experienced high degrees of fractional melting, and three Xuan Loc type-R xenoliths measured for radiogenic isotopes have both very consistent and relatively enriched isotopic signatures (e.g., moderately unradiogenic $^{143}Nd/^{144}Nd$ = 0.512755-0.512800), in agreement with the previously published type-R xenolith from Dalat (0.512766; Nguyen & Kil, 2020). It is thus possible that the relatively shallow, type-R xenoliths are samples of an older lithospheric mantle that has now been partially removed (i.e., eroded or delaminated), consistent with past interpretations.

However, we note the presence of intermediate and even overlapping compositions and depths between the type-R and type-F groups, suggesting the distribution is not truly bimodal. This pattern, revealed by the compilation of more recent, larger data sets (Anh et al., 2021; Nguyen & Kil 2019, 2020) and this study, argues against the presence of such distinct regional layering and such a dramatic, wholesale lithospheric replacement scenario. While the ages and origins of Indochinese type-R and type-F xenoliths are uncertain, we posit that a single, major metasomatic episode has recently modified the entire lithospheric layer, but that metasomatic overprinting of prior geochemical signatures was incomplete. This scenario is most consistent with the observed geochemical correlations shown in Figure 5, which suggest one major metasomatic episode. The likely metasomatic agent is most consistent with infiltration and melt-rock reaction by Cenozoic magmas, indicating that metasomatism has been a recent event that may be particularly localized beneath the major Cenozoic volcanic centers.

We thus suggest an internally consistent, working model for the evolution and tectonic history of the lithospheric mantle beneath Vietnam and Indochina. In our model, the prior presence of both fertile and refractory mantle beneath Vietnam may not require a history of lithospheric removal and replacement, although the trend of generally higher fertility with depth is consistent with a fossil residue of ancient adiabatic upwelling. To place recent events in a tectonic context, during the India-Eurasia collision, Indochina was extruded along the Ailao

Shan-Red River Fault Zone until the tectonic reorganization associated with a change in strike-slip sense along that fault zone and the coeval cessation of rifting in the South China Sea/East Vietnam Sea (Li et al., 2015; Zhu et al., 2009). Following that reorganization, the Sundaland block, which includes Indochina, lacked a “free surface” into which it could continue to laterally extrude due to the tectonic position of Borneo. It is unclear why such a scenario may have simultaneously induced such voluminous (70,000 km^2) tholeiitic basalt production through mantle decompression, but one explanation is that the loss of a free surface during extrusion could have caused coupled lateral flow of the underlying asthenosphere to encounter an opposing mantle flow boundary beneath Borneo, triggering local upwelling and partial melting. Alternately or concurrently, the prior subduction and eventual sinking of the Pacific crustal slab under Indochina may have induced local upper mantle upwelling, as suggested by Yu et al. (2017b). Upwelling of the asthenosphere then resulted in small degrees of decompression melting, causing metasomatism of the overlying mantle lithosphere. This scenario would ultimately produce a relatively heterogeneous SCLM that partially preserves an older history of variable melt removal, but with metasomatic overprinting, perhaps especially under active Cenozoic volcanic centers. Although only one possible scenario, our working model can explain the timing and geochemical compositions of Indochina basalts and xenoliths, in a way that is consistent with local tectonics.

6. Conclusions

In this study, we have characterized two suites of lithospheric mantle xenoliths from southern Vietnam. The measured major elements of peridotite mineral separates, trace elements of cpx and opx, and radiogenic isotope compositions of clinopyroxene in mantle peridotite xenoliths from two sites, Pleiku and Xuan Loc, provide the following insights into the lithospheric mantle of Vietnam:

1. The lithospheric mantle beneath Vietnam experienced a complex history of variable partial melting and subsequent metasomatism, which is preserved in lithospheric mantle-derived spinel peridotites.
2. Type-F or “fertile” spinel peridotites from Pleiku, Xuan Loc, and Dalat based on their spinel Cr#, exhibit fertile compositions with depleted, enriched, and spoon-shaped REE_{PM} patterns indicative of a lithosphere that has undergone low degrees of prior partial melting, and subsequently, variable degrees of silicate melt metasomatism. Type-F xenoliths from all three field locations have calculated equilibration temperatures and pressures that cover a wide range (Anh et al., 2021; Nguyen & Kil, 2019, 2020).
3. Similar to comparable xenoliths from previous work (Nguyen and Kil, 2019, 2020), type-R or “refractory” spinel peridotite xenoliths from Xuan Loc display refractory compositions with enriched and S-shaped REE_{PM} patterns, which indicate high degrees of partial melting followed by pervasive metasomatic enrichment, and share characteristics typical of ancient refractory SCLM. Calculated equilibration pressures for type-R xenoliths are notably restricted to relatively shallow equilibration depths.
4. The dramatic lithospheric erosion and replacement suggested by prior studies (e.g., Anh et al., 2021) may not in fact be necessary to explain Vietnam xenolith compositions. Regardless of the lithospheric mantle’s more ancient origins, however, we posit that the underlying asthenosphere has recently upwelled and experienced decompression partial melting, both metasomatizing the overlying lithospheric mantle and producing extensive local basalt flows.

ACKNOWLEDGMENTS

We acknowledge three anonymous reviewers for providing helpful feedback that strengthened this manuscript. We would like to thank Aaron Satkoski, Staci Loewy, Nate Miller, and Phil Orlandini for assistance in conducting major and trace element and isotopic analyses. Dinh Q. Sang, Le Duc Anh, Nguyen T. Mai, and Tran T. Huong assisted in fieldwork and sample collection in Vietnam, and Nicholas Richard assisted with some of the sample preparation and local map figures. This project was supported by a University of Nebraska-Lincoln College of Arts and Sciences international collaboration award and by NSF EAR-Tectonics award 1758972.

Data availability statement

Supporting data for this study are available in the data supplement provided, and in the EarthChem repository has three linked data sets (Hobbs et al., 2003a, 2003b, 2003c).

REFERENCES

Anh, H.T.H., Choi, S.H., Yu, Y., & Hieu, P.T. (2021). Geochemical constraints on the evolution of the lithospheric mantle beneath central and southern Vietnam. *Geosciences Journal* **25**(4), 433-451, doi:10.1007/s12303-020-0045-4.

Arai, S. (1994). Characterization of spinel peridotites by olivine-spinel compositional relationships: review and interpretation. *Chemical geology* **113**(3-4), 191-204.

Armstrong, J.T. (1988). Quantitative analysis of silicate and oxide materials: comparison of Monte Carlo, ZAF, and $\phi(\rho Z)$ procedures. *Microbeam Analysis,* 239–246.

Baker, J., Peate, D., Waight, T., & Meyzen, C. (2004). Pb isotopic analysis of standards and samples using a ^{207}Pb–^{204}Pb double spike and thallium to correct for mass bias with a double-focusing MC-ICP-MS. *Chemical Geology* **211**(3-4), 275-303.

Ballhaus, C., Berry, R.F., & Green, D.H. (1991). High pressure experimental calibration of the olivine-orthopyroxene-spinel oxygen geobarometer: implications for the oxidation state of the upper mantle. *Contributions to Mineralogy and Petrology* **107**, 27–40, doi:10.1007/BF00311183.

Brey, G.P. & Kohler, T. (1990). Geothermobarometry in Four-phase Lherzolites II. New Thermobarometers, and Practical Assessment of Existing Thermobarometers. *Journal of Petrology* **31**, 1353–1378, doi:10.1093/petrology/31.6.1353.

Byerly, B.L. & Lassiter, J.C. (2012). Evidence from mantle xenoliths for lithosphere removal beneath the central Rio Grande Rift. *Earth and Planetary Science Letters* **355–356**, 82–93, doi:10.1016/j.epsl.2012.08.034.

Byerly, B.L. & Lassiter, J.C. (2015). Trace element partitioning and Lu–Hf isotope systematics in spinel peridotites from the Rio Grande Rift and Colorado Plateau: Towards improved age assessment of clinopyroxene Lu/Hf–^{176}Hf/^{177}Hf in SCLM peridotite. *Chemical Geology* **413**, 146–158, doi:10.1016/j.chemgeo.2015.08.009.

Cipriani, A., Bonatti, E., & Carlson, R.W. (2011). Nonchondritic ^{142}Nd in suboceanic mantle peridotites. *Geochemistry, Geophysics, Geosystems* **12**, doi:10.1029/2010GC003415.

Chu, Z.-Y., Wu, F.-Y., Walker, R.J., Rudnick, R.L., Pitcher, L., Puchtel, I.S., Yang, Y.-H., Wilde, S.A. (2009), Temporal Evolution of the Lithospheric Mantle benath the Eastern North China Craton. *Journal of Petrology* **50** (10), 1857-1898.

Coltorti, M., Bonadiman, C., Hinton, R.W., Siena, F., & Upton, B.G.J. (1999). Carbonatite Metasomatism of the Oceanic Upper Mantle: Evidence from Clinopyroxenes and Glasses in Ultramafic Xenoliths of Grande Comore, Indian Ocean. *Journal of Petrology* **40**, 133–165, doi:10.1093/petroj/40.1.133.

Connelly, J.N., Ulfbeck, D.G., Thrane, K., Bizzarro, M., Housh, T. (2006). A method for pyrifying Lu and Hf for analyses by MC-ICP-MS using TODGA resin. *Chemical Geology* **233**(1-2), 126-136.

Cullen, A., Reemst, P., Henstra, G., Gozzard, S., & Ray, A. (2010). Rifting of the South China Sea: new perspectives. *Petroleum Geoscience* **16**, 273–282, doi:10.1144/1354-079309-908.

Dawson, J.B. (1984). Contrasting Types of Upper-Mantle Metasomatism?, in Kornprobst, J., Ed., *Developments in Petrology,* 289–294, Elsevier. doi:10.1016/B978-0-444-42274-3.50030-5.

Flower, M., Tamaki, K., & Hoang, N. (1998). Mantle extrusion: A model for dispersed volcanism and DUPAL-like asthenosphere in East Asia and the western Pacific, in Flower, M.F.J., Chung, S., Lo, C., and Lee, T., Eds., *Geodynamics Series* **27**, 67–88, American Geophysical Union, Washington, DC. doi:10.1029/GD027p0067.

Frey, F.A. & Green, D.H. (1974). The mineralogy, geochemistry and origin of Iherzolite inclusions in Victorian basanites. *Geochimica et Cosmochimica Acta* **38**, 1023–1059, doi:10.1016/0016-7037(74)90003-9.

Frey, F.A. & Prinz, M. (1978). Ultramafic inclusions from San Carlos, Arizona: Petrologic and geochemical data bearing on their petrogenesis. *Earth and Planetary Science Letters* **38**, 129–176, doi:10.1016/0012-821X(78)90130-9.

Gale, A., Dalton, C.A., Langmuir, C.H., Su, Y., & Schilling, J.-G. (2013). The mean composition of ocean ridge basalts. *Geochemistry Geophysics Geosystems* **14**(3), doi:10.1029/2012GC004334.

Gast, P.W. (1968). Trace element fractionation and the origin of tholeiitic and alkaline magma types. *Geochimica et Cosmochimica Acta* **32**, 1057–1086, doi:10.1016/0016-7037(68)90108-7.

Gibbons, A.D., Zahirovic, S., Müller, R.D., Whittaker, J.M., & Yatheesh, V. (2015). A tectonic model reconciling evidence for the collisions between India, Eurasia and intra-oceanic arcs of the central-eastern Tethys. *Gondwana Research* **28**, 451–492, doi:10.1016/j.gr.2015.01.001.

Griffin, W.L., O'Reilly, S.Y., Afonso, J.C., & Begg, G.C. (2008). The Composition and Evolution of Lithospheric Mantle: A Re-evaluation and its Tectonic Implications. *Journal of Petrology* **50**, 1185–1204, doi:10.1093/petrology/egn033.

Hall, R. (2002). SE Asian heatflow: call for new data. *SEAPEX press* **5**, 54–56.

Hart, S.R. (1984). A large-scale isotope anomaly in the Southern Hemisphere mantle. *Nature* **309**, 753–757, doi:10.1038/309753a0.

Hasterok, D. & Chapman, D.S. (2011). Heat production and geotherms for the continental lithosphere. *Earth and Planetary Science Letters* **307**, 59–70, doi:10.1016/j.epsl.2011.04.034.

Hellebrand, E., Snow, J.E., Dick, H.J.B., & Hofmann, A.W. (2001). Coupled major and trace elements as indicators of the extent of melting in mid-ocean-ridge peridotites. *Nature* **410**, 677–681, doi:10.1038/35070546.

Herzberg, C. (1999). Phase equilibrium constraints on the formation of cratonic mantle: Mantle Petrology: Field Observations and High Pressure Experimentation, *Special Publications* **6**, 241–257, Geochemical Society.

Hieu, P.T., Dung, N.T., Nguyen, T.B.T., Minh, N.T., Minh, P. (2016). U-Pb ages and Hf isotopic composition of zircon and bulk rock geochemistry of the Dai Loc granitoid complex in Kontum massif: Implications for early Paleozoic crustal evolution in Central Vietnam. *Journal of Mineralogical and Petrological Sciences* **111**(5), 326-336, doi: 10.2465/jmps.151229.

Hieu, P.T., Minh, P., Lei, W.X., Quynh Nong, A.T., Kawaguchi, K., Cuong, T.C. (2022). Zircon U-Pb geochronology and Sr-Nd-Hf isotopic compositions of the felsic dykes from the Dalat zone, southern Vietnam: petrogenesis and geological significance. *International Geology Review* **64**(19), 2822-2836, doi: 10.1080/00206814.2021.2015632.

Hoang, N. & Flower, M. (1998). Petrogenesis of Cenozoic Basalts from Vietnam: Implication for Origins of a ‘Diffuse Igneous Province’. *Journal of Petrology* **39**, 369–395, doi:10.1093/petroj/39.3.369.

Hoang, N., Flower, M.F.J. & Carlson, R.W. (1996). Major, trace element, and isotopic compositions of Vietnamese basalts: Interaction of hydrous EM1-rich asthenosphere with thinned Eurasian lithosphere. *Geochimica et Cosmochimica Acta* **60**, 4329–4351, doi:10.1016/S0016-7037(96)00247-5.

Hoang, N., Flower, M.F.J., Chi, C.T., Xuan, P.T., Quy, H.V. & Son, T.T. (2013). Collision-induced basalt eruptions at Pleiku and Buôn Mê Thuột, south-central Viet Nam. *Journal of Geodynamics,* **69**, 65–83, doi:10.1016/j.jog.2012.03.012.

Hoang, N., Shinjo, R., Phuc, L.T., Anh, L.D., Huong, T.T., Pécskay, Z., Bac, D.T. (2019). *Journal of Asian Earth Sciences* **181**, 103903, doi: 10.1016/j.jseaes.2019.103903.

Hobbs, K., Elkins, L. J., Lassiter, J. C., Hoang, N., Burberry, C. M., (2023a). Lithospheric mantle xenolith geochemistry from south-central Vietnam: Trace elements, Version 1.0 [Dataset]. Interdisciplinary Earth Data Alliance (IEDA). doi.org/10.26022/IEDA/112849.

Hobbs, K., Elkins, L. J., Lassiter, J. C., Hoang, N., Burberry, C. M., (2023b). Lithospheric mantle xenolith geochemistry from south-central Vietnam: Radiogenic isotopes, Version 1.0 [Dataset]. Interdisciplinary Earth Data Alliance (IEDA). doi.org/10.26022/IEDA/112848.

Hobbs, K., Elkins, L. J., Lassiter, J. C., Hoang, N., Burberry, C. M., (2023c). Lithospheric mantle xenolith geochemistry from south-central Vietnam: Major elements, Version 1.0 [Dataset]. Interdisciplinary Earth Data Alliance (IEDA). doi.org/10.26022/IEDA/112847.

Hofmann, A.W. (2007). Sampling Mantle Heterogeneity through Oceanic Basalts: Isotopes and Trace Elements, in Carlson, R.W., Holland, H.D., and Turekian, K.K., Eds., *Treatise on Geochemistry: The Mantle and Core*, 61–101. Elsevier, New York.

Ionov, D.A. (2002). Mechanisms and Sources of Mantle Metasomatism: Major and Trace Element Compositions of Peridotite Xenoliths from Spitsbergen in the Context of Numerical Modelling. *Journal of Petrology* **43**, 2219–2259, doi:10.1093/petrology/43.12.2219.

Johnson, K.T.M., Dick, H.J.B., & Shimizu, N. (1990). Melting in the oceanic upper mantle: An ion microprobe study of diopsides in abyssal peridotites. *Journal of Geophysical Research* **95**, 2661, doi:10.1029/JB095iB03p02661.

Jolivet, L., Faccenna, C., Becker, T., Tesauro, M., Sternai, P., & Bouilhol, P. (2018). Mantle Flow and Deforming Continents: From India-Asia Convergence to Pacific Subduction. *Tectonics* **37**, 2887–2914, doi:10.1029/2018TC005036.

Lassiter, J.C., Blichert-Toft, J., Hauri, E.H., & Barsczus, H.G. (2003). Isotope and trace element variations in lavas from Raivavae and Rapa, Cook–Austral islands: constraints on the nature of HIMU- and EM-mantle and the origin of mid-plate volcanism in French Polynesia. *Chemical Geology* **202**, 115–138, doi:10.1016/j.chemgeo.2003.08.002.

Li, C.-F., Li, J., Ding, W., Franke, D., Yao, Y., Shi, H., Pang, X., Cao, Y., Lin, J., Kulhanek, D.K., & Williams, T. (2015). Seismic stratigraphy of the central South China Sea basin and implications for neotectonics. *Journal of Geophysical Research: Solid Earth* **120**, 1377–1399, doi:10.1002/2014JB011686.

Liang, Y., Sun, C., & Yao, L. (2013). A REE-in-two-pyroxene thermometer for mafic and ultramafic rocks. *Geochimica et Cosmochimica Acta* **102**, 246–260, doi:10.1016/j.gca.2012.10.035.

Liermann, H.P. & Ganguly, J. (2003). Fe^{2+}–Mg fractionation between orthopyroxene and spinel: experimental calibration in the system FeO–MgO–Al_2O_3–Cr_2O_3–SiO_2, and applications. *Contributions to Mineralogy and Petrology* **145**, 217–227, doi:10.1007/s00410-003-0444-3.

Liu, J., Carlson, R.W., Rudnick, R.L., Walker, R.J., Gao, S., & Wu, F. (2012). Comparative Sr–Nd–Hf–Os–Pb isotope systematics of xenolithic peridotites from Yangyuan, North China Craton: Additional evidence for a Paleoproterozoic age. *Chemical Geology* **332–333**, 1–14, doi:10.1016/j.chemgeo.2012.09.013.

Loubet, M., Shimizu, N., & Allègre, C.J. (1975). Rare earth elements in alpine peridotites. *Contributions to Mineralogy and Petrology* **53**, 1–12, doi:10.1007/BF00402450.

Mallick, S., Dick, H.J.B., Sachi-Kocher, A., & Salters, V.J.M. (2014). Isotope and trace element insights into heterogeneity of subridge mantle. *Geochemistry, Geophysics, Geosystems* **15**, 2438–2453, doi:10.1002/2014GC005314.

McDonough, W.F. (1990). Constraints on the composition of the continental lithospheric mantle. *Earth and Planetary Science Letters* **101**, 1–18, doi:10.1016/0012-821X(90)90119-I.

Metcalfe, I. (2013). Gondwana dispersion and Asian accretion: Tectonic and palaeogeographic evolution of eastern Tethys. *Journal of Asian Earth Sciences* **66**, 1–33, doi:10.1016/j.jseaes.2012.12.020.

Michael, P.J. & Bonatti, E. (1985). Peridotite composition from the North Atlantic: regional and tectonic variations and implications for partial melting. *Earth and Planetary Science Letters* **73**, 91–104, doi:10.1016/0012-821X(85)90037-8.

Navon, O. & Stolper, E. (1987). Geochemical Consequences of Melt Percolation: The Upper Mantle as a Chromatographic Column. *The Journal of Geology* **95**, 285–307, doi:10.1086/629131.

Nguyen P.H., Bui, Q.C., & Nguyen, X.D. (2012). Investigation of earthquake tsunami sources, capable of affecting Vietnamese coast. *Natural Hazards* **64**, 311-327.

Nguyen, T.C. & Kil, Y. (2019). The evolution of the lithospheric mantle beneath Ia Bang, Pleiku plateau, Central Vietnam. *Journal of Asian Earth Sciences* **174**, 232–244, doi:10.1016/j.jseaes.2018.12.011.

Nguyen, C. & Kil, Y. (2020). Petrological characteristics of lithospheric mantle beneath Nui Nua and Ba Ria areas, southern Vietnam. *Geosciences Journal* **24**(5), 475-487, doi:10.1007/s12303-020-0017-8.

Pan, S., Zheng, J., Chu, L., & Griffin, W.L. (2013). Coexistence of the moderately refractory and fertile mantle beneath the eastern Central Asian Orogenic Belt. *Construction and Destruction of Cratons* **23**, 176–189, doi:10.1016/j.gr.2012.03.001.

Patchett, P.J. & Tatsumoto, M. (1980). Hafnium isotope variations in oceanic basalts. *Geophysical Research Letters* **7**(12), 1077-1080.

Phach, P.V. & Anh, L.D. (2018). Tectonic evolution of the southern part of Central Viet Nam and the adjacent area. *Geodynamics & Tectonophysics* **9**, 801–825, doi:10.5800/GT-2018-9-3-0372.

Putirka, K.D. (2008). Thermometers and Barometers for Volcanic Systems. *Reviews in Mineralogy and Geochemistry* **69**, 61–120, doi:10.2138/rmg.2008.69.3.

Rohrmann, A., Kapp, P., Carrapa, B., Reiners, P.W., Guynn, J., Ding, L., & Heizler, M. (2012). Thermochronologic evidence for plateau formation in central Tibet by 45 Ma. *Geology* **40**, 187–190, doi:10.1130/G32530.1.

Royden, L.H., Burchfiel, B.C., & van der Hilst, R.D. (2008). The Geological Evolution of the Tibetan Plateau. *Science* **321**, 1054–1058, doi:10.1126/science.1155371.

Rudnick, R.L. & Fountain, D.M. (1995). Nature and composition of the continental crust: A lower crustal perspective. *Reviews of Geophysics* **33**, 267–309, doi:10.1029/95RG01302.

Salters, V.J.M. & Stracke, A. (2004). Composition of the depleted mantle. *Geochemistry, Geophysics, Geosystems* **5**, doi:10.1029/2003GC000597.

Sanfilippo, A., Salters, V.J.M., Sokolov, S.Y., Peyve, A.A., Stracke, A. (2021). Ancient refractory asthenosphere revealed by mantle re-melting at the Artic Mid Atlantic Ridge. *Earth and Planetary Science Letters* **566**, 116981, doi: 10.1016/j.epsl.2021.116981.

Scott, J.M., Hodgkinson, A., Palin, J.M., Waight, T.E., Van der Meer, Q.H.A., & Cooper, A.F. (2014). Ancient melt depletion overprinted by young carbonatitic metasomatism in the New Zealand lithospheric mantle. *Contributions to Mineralogy and Petrology* **167**, 963, doi:10.1007/s00410-014-0963-0.

Shaw, D.M. (1970). Trace element fractionation during anatexis. *Geochimica et Cosmochimica Acta* **34**, 237–243, doi:10.1016/0016-7037(70)90009-8.

Shellnutt, J.G., Lan, C.-Y., Van Long, T., Usuki, T., Yang, H.-J., Mertzman, S.A., Iizuka, Y., Chung, S.-L., Wang, K.-L., & Hsu, W.-Y. (2013). Formation of Cretaceous Cordilleran and post-orogenic granites and their microgranular enclaves from the Dalat zone, southern Vietnam: Tectonic implications for the evolution of Southeast Asia. *Lithos* **182–183**, 229–241, doi:10.1016/j.lithos.2013.09.016.

Sims, K. W., Hart, S. R., Reagan, M. K., Blusztajn, J., Staudigel, H., Sohn, R. A., Layne, G.D., Ball, L.A., & Andrews, J. (2008). ^{238}U-^{230}Th-^{226}Ra-^{210}Pb-^{210}Po, ^{232}Th-^{228}Ra, and ^{235}U-^{231}Pa constraints on the ages and petrogenesis of Vailulu'u and Malumalu Lavas, Samoa. *Geochemistry, Geophysics, Geosystems* **9**(4), https://doi.org/10.1029/2007GC001651.

Stracke, A., Snow, J.E., Hellebrand, E., von der Handt, A., Bourdon, B., Birbaum, K., & Günther, D. (2011). Abyssal peridotite Hf isotopes identify extreme mantle depletion. *Earth and Planetary Science Letters* **308**, 359–368, doi:10.1016/j.epsl.2011.06.012.

Sun, S-S. & McDonough, W.F. (1989). Chemical and isotopic systematics of oceanic basalts: implications for mantle composition and processes. *Special Publications* **42**, 313–345, doi:10.1144/GSL.SP.1989.042.01.19. Geological Society, London.

Tapponnier, P., Lacassin, R., Leloup, P.H., Shärer, U., Dalai, Z., Haiwei, W., Xiaohan, L., Shaocheng, J., Lianshang, Z., and Jiayou, Z., 1990. The Ailao Shan/Red River metamorphic belt: Tertiary left-lateral shear between Indochina and South China. *Nature* **343** (6257), 431–437, doi: 10.1038/343431a0.

Tapponnier P., Peltzer G., Armijo R., 1986. On the mechanics of the collision between India and Asia. In, Coward, M.P., Ries, A.C. (Eds.), Collision Tectonics, *Special Publications* **19**, 115-157. Geological Society of London.

Toramaru, A. & Fujii, N. (1986). Connectivity of melt phase in a partially molten peridotite. *Journal of Geophysical Research: Solid Earth* **91**, 9239–9252, doi:10.1029/JB091iB09p09239.

Tu, K., Flower, K.F.J., Carlson, R.W., Zhang, M., Xie, G. (1991). Sr, Nd, and Pb isotopic compositions of Hainan basalts (south China): Implications for a subcontinental lithosphere Dupal source. *Geology* **19**, 567-569.

Tu, K., Flower, M.F.J., Carlson, R.W., Xie, G., Chen, C.-Y., Zhang, M. (1992). Magmatisn in the South China Basin: 1. Isotopic and trace element evidence for an endogenous Dupal mantle component. *Chemical Geology* **97**, 47-63.

Turcotte, D. & Schubert, G. (2002). *Geodynamics,* Cambridge University Press, Cambridge, UK, pp. 472. doi:10.1017/CBO9780511807442.

Vervoort, J.D., Patchett, P.J., Blichert-Toft, J., Albarede, F. (1999). Relationships between Lu-Hf and Sm-Nd isotopic systems in the global sedimentary system. *Earth and Planetary Science Letters* **168**(1-2), 79-99, doi: 10.1016/s0012-821x(99)00047-3.

Warren, J.M. (2016) Global variations in abyssal peridotite compositions. *Lithos* **248–251**, 193–219, doi:10.1016/j.lithos.2015.12.023.

Workman, R.K. & Hart, S.R. (2005). Major and trace element composition of the depleted MORB mantle (DMM). *Earth and Planetary Science Letters* **231**, 53–72, doi:10.1016/j.epsl.2004.12.005.

Workman, R. K., Hart, S. R., Jackson, M., Regelous, M., Farley, K. A., Blusztajn, J., Kurz, M., & Staudigel, H. (2004). Recycled metasomatized lithosphere as the origin of the Enriched Mantle II (EM2) end-member: Evidence from the Samoan Volcanic Chain. *Geochemistry, Geophysics, Geosystems* **5**(4), https://doi.org/10.1029/2003GC000623.

Yu, Y., Hung, T.D., Yang, T., Xue, M., Liu, K.H., & Gao, S.S. (2017). Lateral variations of crustal structure beneath the Indochina Peninsula. *Tectonophysics* **712–713**, 193–199, doi:10.1016/j.tecto.2017.05.023.

Yu, Y., Gao, S.S., Liu, K.H., Yang, T., Xue, M., & Le, K.P. (2017), Mantle transition zone discontinuities beneath the Indochina Peninsula: Implications for slab subduction and mantle upwelling. *Geophysical Research Letters* **44**(14), 7159-7167, doi:10.1002/2017GL073528.

Zhu, M., Graham, S., & McHargue, T. (2009). The Red River Fault zone in the Yinggehai Basin, South China Sea. *Tectonophysics* **476**, 397–417, doi:10.1016/j.tecto.2009.06.015.

FIGURE CAPTIONS

Figure 1. a. Map of southern and southeast Asia, illustrating extrusion of Indochina due to the India-Eurasia collision (gray arrows) (after Taponnier et al., 1986, 1990). “Red river” = Ailao Shan-Red River Fault Zone. **b.** Map of study area and sample collection localities. Major mapped faults and volcanic centers are modified from published literature (Hoang et al., 1996, 2013; Nguyen et al., 2012; Phach & Anh, 2018).

Figure 2. a. Clinopyroxene Al_2O_3 rim/core ratio versus cpx Cr_2O_3 rim/core ratio. **b.** Orthopyroxene Al_2O_3 rim/core ratio versus cpx Cr_2O_3 rim/core ratio. Other parameters such as Mg# and Cr# show similar strong positive correlations in most samples. **c.** Cpx core Al_2O_3 wt% vs. cpx Mg# (molar Mg/(Mg + Fe)). Small symbols show published xenolith data from Pleiku (Nguyen & Kil, 2019) and Dalat (Anh et al., 2021; Nguyen & Kil, 2020).

Figure 3. Rare earth and trace element concentrations of samples from this study normalized to primitive mantle (Sun and McDonough, 1989). Gray solid lines show type-F xenoliths and gray dashed lines show type-R xenoliths from Pleiku and Dalat (Anh et al., 2021; Nguyen and Kil, 2019, 2020). Shaded grey fields show the range of cpx compositions in abyssal peridotites (Warren, 2016), except where noted otherwise. **a.** Clinopyroxene rare earth element concentrations for type-F Pleiku peridotites (solid blue lines), with Pleiku xenoliths from Nguyen and Kil (2019) shown as solid (type-F) and dashed (type-R) gray lines for comparison. **b.** Clinopyroxene rare earth element concentrations for Xuan Loc peridotites, where type-R peridotites are shown by dashed and type-F peridotites by solid red lines; Dalat xenoliths from Ang et al. (2021) and Nguyen and Kil (2020) are shown as solid (type-F) and dashed (type-R) gray lines for comparison. **c.** Clinopyroxene trace element concentrations for Pleiku peridotite xenoliths from this study; **d.** cpx trace element concentrations of Xuan Loc peridotites from this study; and **e.** opx trace element concentrations of both Pleiku and Xuan Loc peridotites from this study; the grey field represents the detection limits for each element.

Figure 4. a. $^{207}Pb/^{204}Pb$ and **c.** $^{208}Pb/^{204}Pb$ versus $^{206}Pb/^{204}Pb$; **b.** $^{206}Pb/^{204}Pb$ and **d.** ε_{Nd} versus $^{87}Sr/^{86}Sr$; **e.** $^{206}Pb/^{204}Pb$ vs. ε_{Nd}; and **f.** ε_{Hf} vs. ε_{Nd} for cpx from Pleiku (blue squares) and Xuan Loc (red circles) peridotites for this study (larger square and circle symbols). Uncertainty ranges (2σ) are smaller than symbol size. Small gray circles show Indian MORB compositions after Gale et al. (2013). Enriched mantle (EM) compositions are after Hofmann (2007), and the northern hemisphere reference line (NHRL) is after Hart (1984). Local basalt compositions from

the Pleiku and Xuan Loc volcanic centers are from Hoang et al. (1996; 2013). Literature data for Pleiku and Dalat xenolith compositions (smaller symbols) are from Anh et al. (2021) and Nguyen and Kil (2019, 2020).

Figure 5. Spinel Cr# vs **a.** Al_2O_3 wt%, **b.** Yb_N, and **c.** [Ti] in cpx; **d.** ε_{Nd} in cpx vs. $(Ce/Yb)_{PM}$ in cpx, and **e.** $^{143}Nd/^{144}Nd$ vs. Sm/Yb in cpx, for Vietnam xenoliths from this study and prior studies (Anh et al., 2021; Nguyen & Kil, 2019, 2020). Low Al_2O_3, low Yb, and high sp Cr# characterize xenoliths that have undergone extensive melt extraction. The dashed line and tickmarks show the calculated degree of melting as a percentage, where the degrees of melting are a function of sp Cr# (Hellebrand et al., 2001) and Yb concentration (Johnson et al., 1990).

Figure 6. Comparison of equilibrium temperatures of Vietnam xenoliths with **a.** T_{36} and **b.** T_{REE} plotted versus T_{BKN}. The uncertainties (1σ) are ± 45 ºC for T_{36}, ±50 °C for T_{BKN} (Putirka, 2008), and as shown with error bars for T_{REE}. Black solid line is the 1:1 ratio, with the dotted lines representing ±50 °C.

Figure 7. a. $^{143}Nd/^{144}Nd$ vs. 1/Nd in cpx for samples from this study. The dashed line shows a simple, representative binary mixing trajectory between a weighted average of Cenozoic Vietnam basalts (Hoang et al., 1996, 2013, 2019) and enriched sample VN-2018-21-PL-2, where the labeled tickmarks indicate the percentage of basalt added to VN-2018-21-PL-2 along the mixing line. **b.** $^{176}Hf/^{177}Hf$ vs. 1/Hf for samples from this study. **c.** $^{143}Nd/^{144}Nd$ vs. calculated model ages for samples from this study, as described in the text and for a DMM evolution curve calculated using the composition of Workman and Hart (2005).

Figure 8. Estimated equilibration temperatures (**a.** T_{36} and **b.** T_{BKN}) and **c.** measured $^{143}Nd/^{144}Nd$ isotopes, versus pressures (P_{38}) for xenolith samples from this study and prior studies (Anh et al., 2021; Nguyen & Kil, 2019, 2020). The calculated geothermal gradients beneath Pleiku and Xuan Loc, which were determined using measured lithospheric thickness and estimated heat flow, are also shown (using heat flow data after Hall (2002), and references therein).

Table 1. Sample locations for this study.

	Latitude (ºN)	Longitude (ºE)	Elevation (ft)	Xenolith type
Pleiku				
VN-2018-21-PL-1	13º 52.582'	108º 3.653'	2602	spinel lherzolite
VN-2018-21-PL-2	13º 52.582'	108º 3.653'	2602	spinel lherzolite
VN-2018-21-PL-3	13º 52.582'	108º 3.653'	2602	spinel lherzolite
VN-2018-21-PL-4	13º 52.582'	108º 3.653'	2602	spinel lherzolite
VN-2018-21-PL-5	13º 52.582'	108º 3.653'	2602	spinel lherzolite
VN-2018-21-PL-6	13º 52.582'	108º 3.653'	2602	spinel lherzolite
VN-2018-21-PL-7	13º 52.582'	108º 3.653'	2602	spinel lherzolite
VN-2018-21-PL-8	13º 52.582'	108º 3.653'	2602	spinel lherzolite
VN-2018-21-PL-9	13º 52.582'	108º 3.653'	2602	spinel lherzolite
Xuan Loc				
VN-2018-36-XL-1	10º 30.457'	107º 16.375'	229	dunite
VN-2018-36-XL-2	10º 30.457'	107º 16.375'	229	harzburgite
VN-2018-36-XL-3	10º 30.457'	107º 16.375'	229	spinel lherzolite
VN-2018-36-XL-4	10º 30.457'	107º 16.375'	229	harzburgite
VN-2018-36-XL-5	10º 30.457'	107º 16.375'	229	dunite
VN-2018-36-XL-7	10º 30.457'	107º 16.375'	229	spinel lherzolite
VN-2018-36-XL-8	10º 30.457'	107º 16.375'	229	spinel lherzolite
VN-2018-36-XL-9	10º 30.457'	107º 16.375'	229	spinel lherzolite
VN-2018-36-XL-11	10º 30.457'	107º 16.375'	229	dunite
VN-2018-36-XL-12	10º 30.457'	107º 16.375'	229	dunite
VN-2018-36-XL-13	10º 30.457'	107º 16.375'	229	harzburgite
VN-2018-36-XL-14	10º 30.457'	107º 16.375'	229	spinel peridotite
VN-2018-36-XL-15	10º 30.457'	107º 16.375'	229	spinel lherzolite
VN-2018-36-XL-16	10º 30.457'	107º 16.375'	229	spinel lherzolite
VN-2018-36-XL-18	10º 30.457'	107º 16.375'	229	spinel lherzolite
VN-2018-36-XL-19	10º 30.457'	107º 16.375'	229	spinel lherzolite
VN-2018-36-XL-20	10º 30.457'	107º 16.375'	229	spinel lherzolite

Table 2. Isotopic composition of Vietnam xenoliths.

	Type	$^{87}Sr/^{86}Sr$	2σ **	$^{143}Nd/^{144}Nd$	2σ**	$^{176}Hf/^{177}Hf$	2σ**	$^{206}Pb/^{204}Pb$	2σ**	$^{207}Pb/^{204}Pb$	2σ**	$^{208}Pb/^{204}Pb$	2σ**
Pleiku													
VN-2018-21-PL-1*	F	0.703267	±5	-	-	-	-	16.92	±1	15.45	±1	36.90	±3
VN-2018-21-PL-2	F	0.703365	±6	0.514190	±7	0.28472	±3	18.859	±2	15.579	±2	38.851	±4
VN-2018-21-PL-3*	F	0.702447	±6	0.513637	±7	0.28371	±1	16.69	±1	15.34	±1	36.48	±3
VN-2018-21-PL-4	F	0.704211	±6	0.512808	±4	-	-	18.33	±2	15.59	±2	38.50	±5
VN-2018-21-PL-5	F	0.702919	±5	0.513091	±4	0.28321	±1	18.591	±2	15.518	±2	38.579	±4
VN-2018-21-PL-6*	F	0.702425	±6	0.513776	±5	-	-	18.29	±1	15.49	±1	38.28	±3
VN-2018-21-PL-7*	F	0.702988	±7	-	-	-	-	17.39	±1	15.48	±1	37.30	±2
VN-2018-21-PL-8	F	0.702463	±6	-	-	-	-	18.1815	±2	15.560	±2	38.202	±5
VN-2018-21-PL-9*	F	0.702381	±5	0.513821	±5	-	-	18.27	±1	15.50	±1	38.27	±3
Xuan Loc													
VN-2018-36-XL-1	R	0.704050	±6	0.512800	±5	-	-	18.179	±2	15.548	±1	38.436	±4
VN-2018-36-XL-3	F	0.702645	±5	0.513196	±5	0.283809	±8	17.348	±2	15.461	±2	37.421	±4
VN-2018-36-XL-5	R	-	-	0.512755	±5	-	-	18.371	±2	15.572	±2	38.640	±5
VN-2018-36-XL-8	F	0.703724	±6	0.512921	±5	-	-	18.284	±2	15.541	±2	38.505	±5
VN-2018-36-XL-9	F	0.703162	±6	0.513036	±5	-	-	17.877	±2	15.494	±1	38.068	±3
VN-2018-36-XL-11	R	-	-	0.512755	±5	-	-	18.317	±2	15.570	±2	38.613	±5
VN-2018-36-XL-14	F	0.702952	±6	0.513176	±4	0.28328	±1	18.019	±2	15.512	±2	38.247	±5
VN-2018-36-XL-15	F	0.702565	±6	0.513358	±12	-	-	17.133	±1	15.435	±1	37.079	±3
VN-2018-36-XL-18	F	0.702995	±6	0.513087	±5	-	-	18.225	±1	15.529	±1	38.413	±3
VN-2018-36-XL-19	F	0.702967	±6	0.513371	±5	-	-	17.874	±2	15.509	±1	38.033	±3
VN-2018-36-XL-20	F	0.703070	±6	0.513110	±5	-	-	18.026	±2	15.520	±1	38.283	±3
Standards													
BCR-2	n = 2	0.705006	±8	0.512639	±5	0.28289	±1	18.756	±2	15.630	±2	38.740	±6
BHVO-2	n = 1	0.703472	±6	0.512987	±4	0.28311	±1	18.619	±2	15.542	±2	38.245	±5
BCR-2***	n = 5							18.76	±1	15.66	±1	38.77	±2
BHVO-2***	n = 5							18.61	±1	15.56	±1	38.20	±2

* Pb-isotopes measured via multi-Daly measurement with sample-standard bracketing

** Uncertainties are 2s internal standard error for the last digit expressed.

*** Pb-isotope measurement via multi-Daly measurement with sample-standard bracketing during same analytical session.

Table 3. Equilibrium temperatures (ºC) and pressures (kbar) of Vietnam xenoliths. *

	Type	T_{BKN}	T_{36}	T_{REE}	1σ	P_{P38}
Pleiku						
VN-2018-21-PL-1	F	912	959	927	±47	11.7
VN-2018-21-PL-2	F	963	956	907	±10	15.8
VN-2018-21-PL-3	F	891	965	926	±25	13.4
VN-2018-21-PL-5	F	1067	1034	993	±30	13.6
VN-2018-21-PL-6	F	958	966	892	±13	15.1
VN-2018-21-PL-7	F	945	945	907	±40	13.1
VN-2018-21-PL-8	F	1000	1008	1032	±18	12.3
VN-2018-21-PL-9	F	967	972	887	±13	15.6
Xuan Loc						
VN-2018-36-XL-2	R	921	1006	-		9.6
VN-2018-36-XL-3	F	856	951	845	±59	12.2
VN-2018-36-XL-4	R	765	942	-		8.1
VN-2018-36-XL-5	R	795	923	1004	±94	7.1
VN-2018-36-XL-7	F	805	940	1076	±63	12.7
VN-2018-36-XL-8	F	859	935	1070	±37	12.1
VN-2018-36-XL-9	F	851	932	861	±49	13.2
VN-2018-36-XL-11	R	927	942	997	±70	10.0
VN-2018-36-XL-14	F	924	936	821	±25	15.3
VN-2018-36-XL-15	F	1026	992	843	±42	16.1
VN-2018-36-XL-18	F	907	927	908	±32	12.6
VN-2018-36-XL-19	F	946	959	916	±31	12.8
VN-2018-36-XL-20	F	894	929	885	±23	13.2

* Major element equilibrium temperatures calculated from the two-pyroxene thermometer (T_{BKN}) of Brey and Kohler (1990). T_{BKN} has an uncertainty (1σ) of ± 50 ºC. Temperatures are also calculated using the two-pyroxene thermometer of Putirka (2008) (T_{36}), with an uncertainty (1σ) of ± 45 ºC. Trace element equilibrium temperatures are calculated from the two-pyroxene REE thermometer (T_{REE}) of Liang et al. (2013); uncertainties reported are from linear fit of the inversion diagrams from that method (see Supplementary Information). Equilibration pressures (P_{38}) are calculated using the two-pyroxene barometer of Putirka (2008), with an uncertainty of ± 3.7 kbar.

Figure 1.

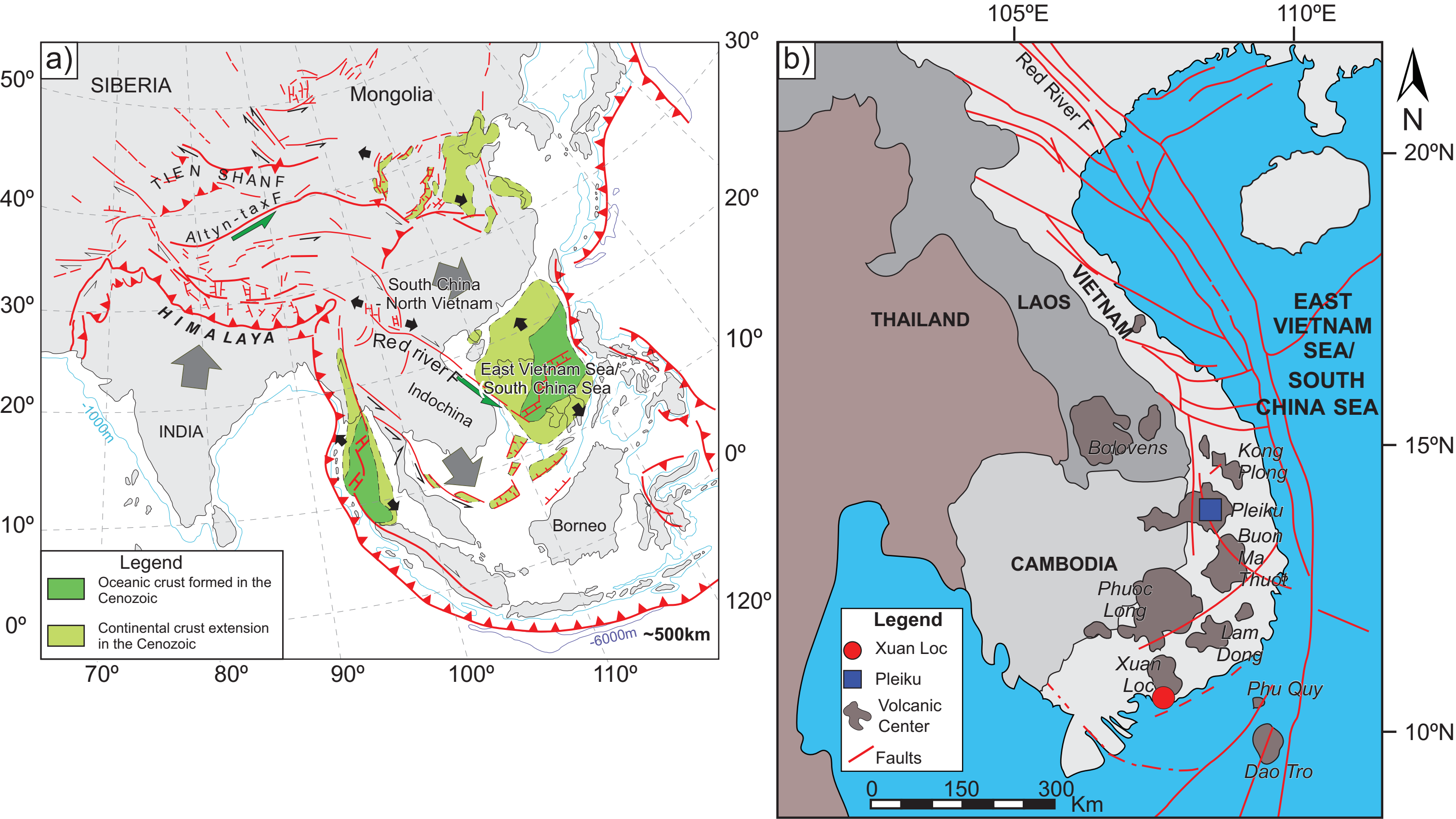

a)
SIBERIA
Mongolia
TIEN SHAN F
Altyn-tax F
HIMALAYA
INDIA
South China - North Vietnam
Red river F
Indochina
East Vietnam Sea/ South China Sea
Borneo
-1000m
-6000m
~500km
Legend
Oceanic crust formed in the Cenozoic
Continental crust extension in the Cenozoic
50º
40º
30º
20º
10º
0º
70º
80º
90º
100º
110º
120º
b)
105ºE
110ºE
20ºN
15ºN
10ºN
N
Red River F
THAILAND
LAOS
VIETNAM
CAMBODIA
EAST VIETNAM SEA/ SOUTH CHINA SEA
Bolovens
Kong Plong
Pleiku
Buon Ma Thuot
Phuoc Long
Lam Dong
Xuan Loc
Phu Quy
Dao Tro
Legend
Xuan Loc
Pleiku
Volcanic Center
Faults
0
150
300
Km

Figure 2.

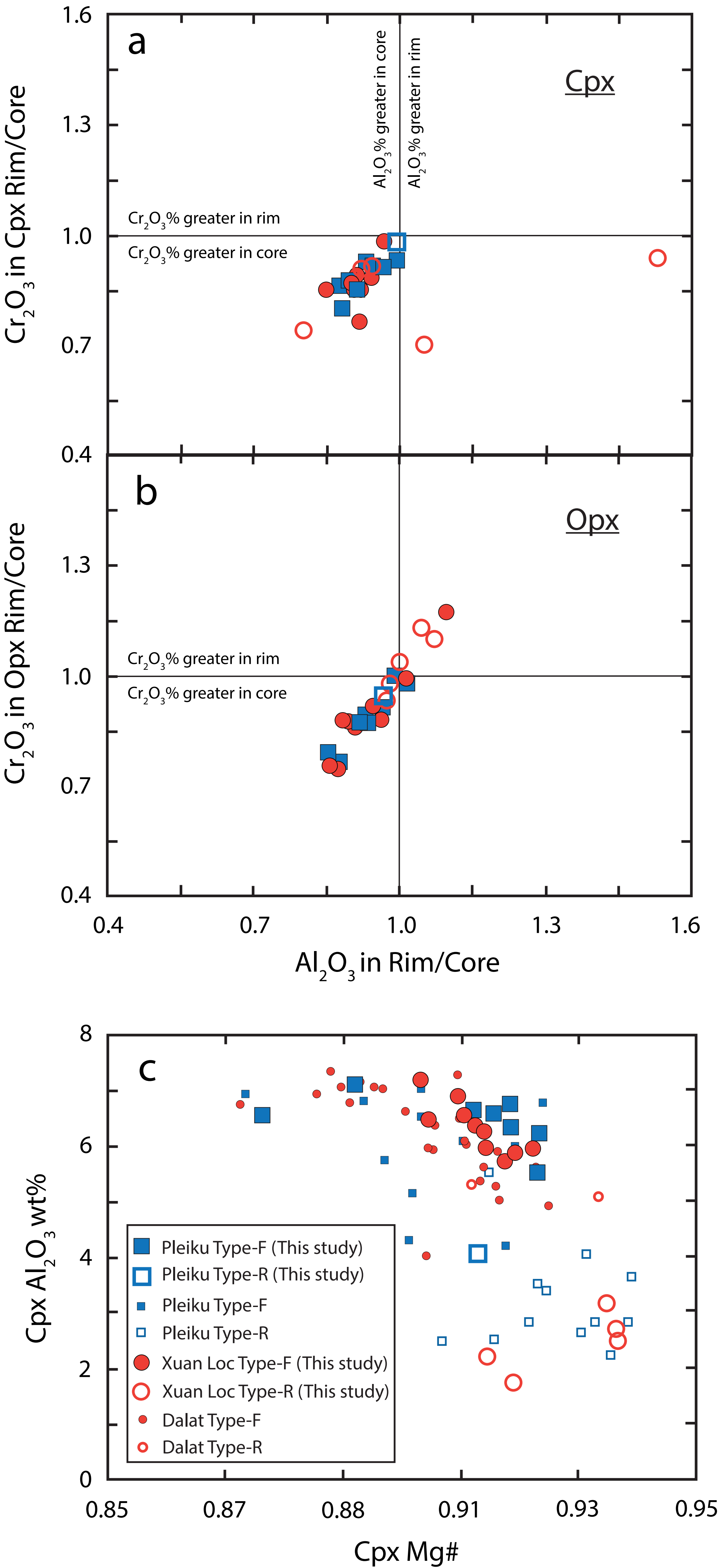
a
Cpx
b
Opx
c
Al_2O_3% greater in core
Al_2O_3% greater in rim
Cr_2O_3% greater in rim
Cr_2O_3% greater in core
Cr_2O_3 in Cpx Rim/Core
Cr_2O_3 in Opx Rim/Core
Al_2O_3 in Rim/Core
Cpx Al_2O_3 wt%
Cpx Mg#
Pleiku Type-F (This study)
Pleiku Type-R (This study)
Pleiku Type-F
Pleiku Type-R
Xuan Loc Type-F (This study)
Xuan Loc Type-R (This study)
Dalat Type-F
Dalat Type-R

Figure 3.

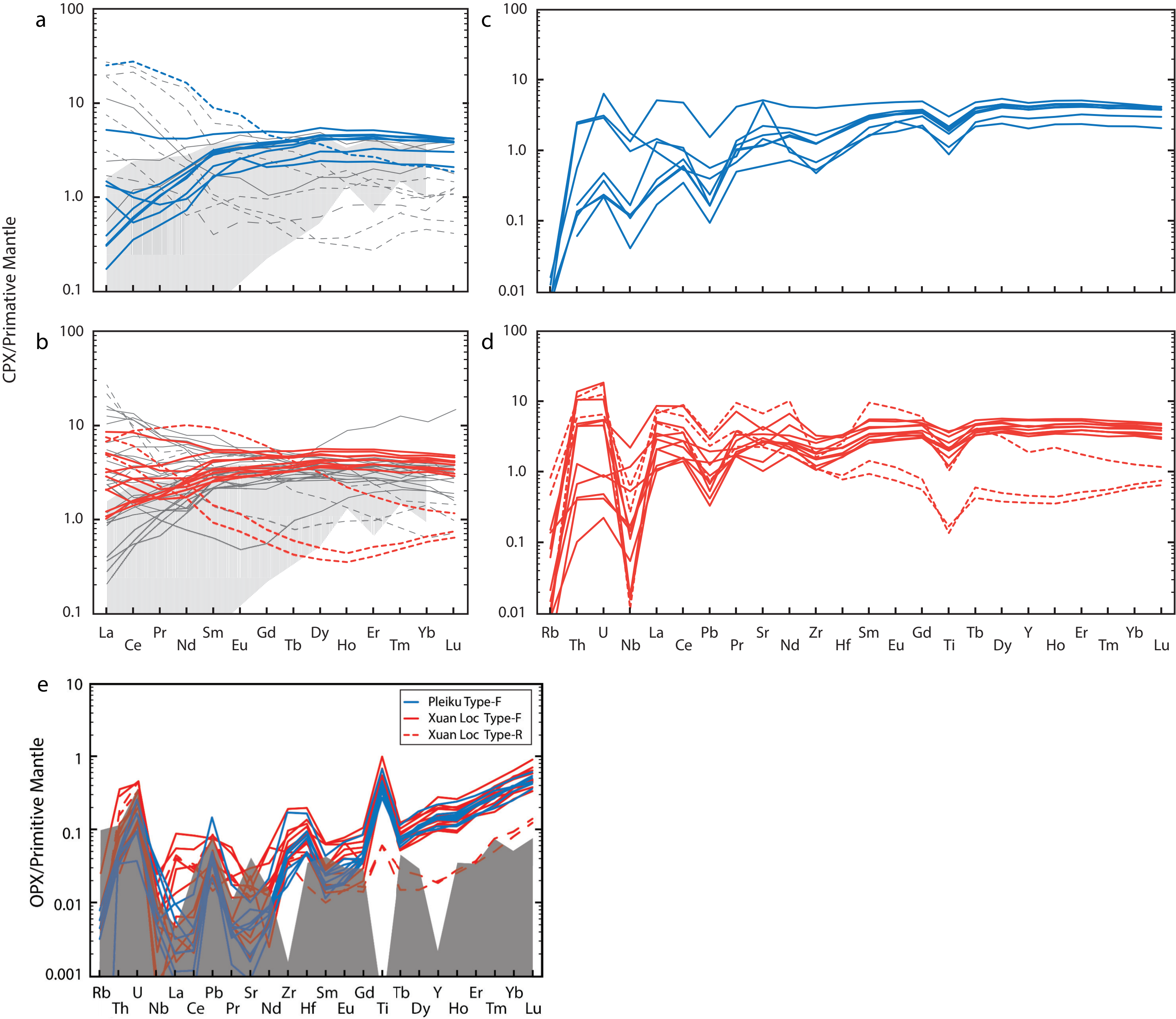
a
b
c
d
e
CPX/Primative Mantle
OPX/Primitive Mantle
100
10
1.0
0.1
0.01
0.001
1
La Ce Pr Nd Sm Eu Gd Tb Dy Ho Er Tm Yb Lu
Rb Th U Nb La Ce Pb Pr Sr Nd Zr Hf Sm Eu Gd Ti Tb Dy Y Ho Er Tm Yb Lu
Pleiku Type-F
Xuan Loc Type-F
Xuan Loc Type-R

Figure 4.

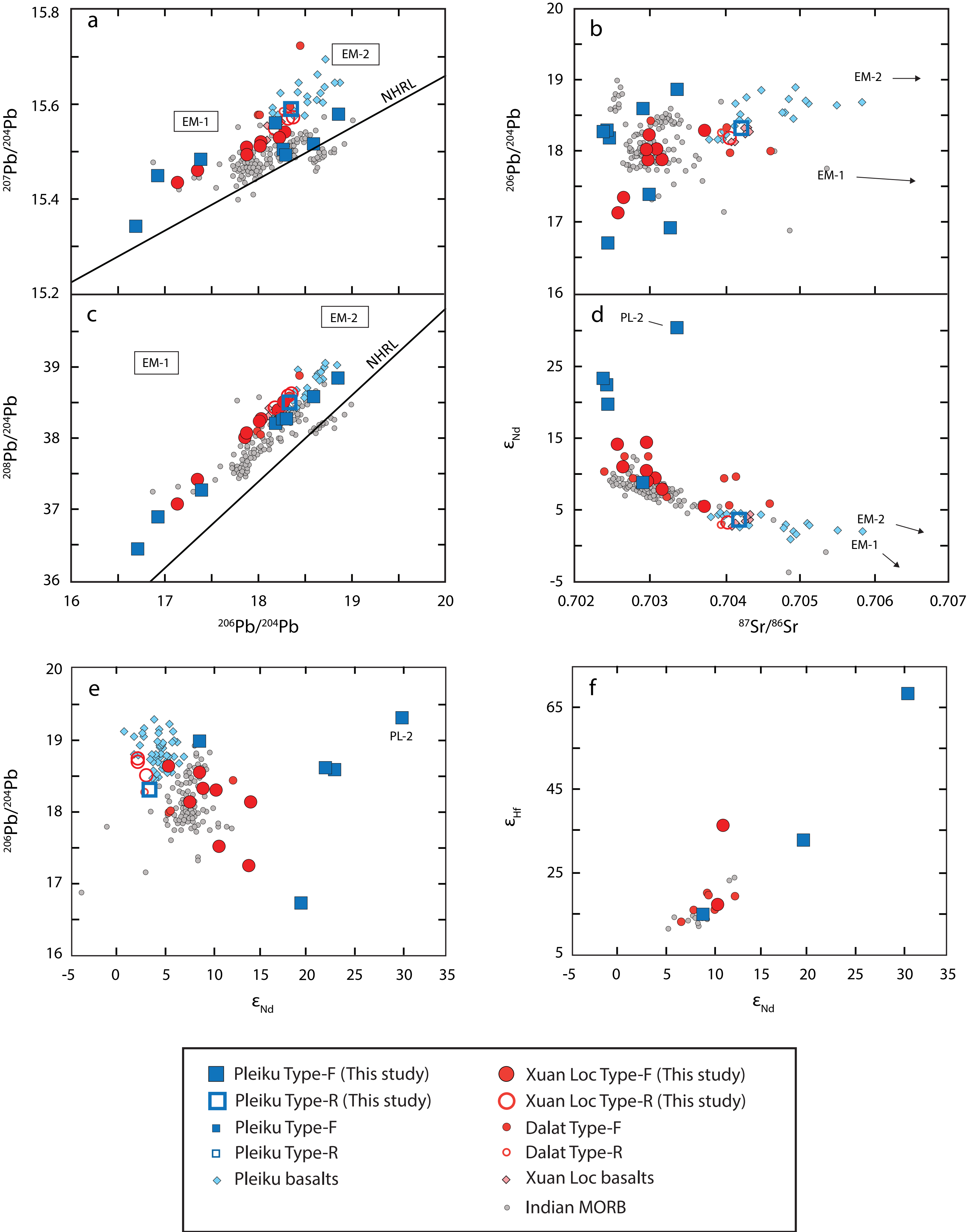

a
EM-2
EM-1
NHRL
$^{207}Pb/^{204}Pb$
b
EM-2
EM-1
$^{206}Pb/^{204}Pb$
c
EM-2
EM-1
NHRL
$^{208}Pb/^{204}Pb$
$^{206}Pb/^{204}Pb$
d
PL-2
EM-2
EM-1
ε_{Nd}
$^{87}Sr/^{86}Sr$
e
PL-2
$^{206}Pb/^{204}Pb$
ε_{Nd}
f
ε_{Hf}
ε_{Nd}
Pleiku Type-F (This study)
Pleiku Type-R (This study)
Pleiku Type-F
Pleiku Type-R
Pleiku basalts
Xuan Loc Type-F (This study)
Xuan Loc Type-R (This study)
Dalat Type-F
Dalat Type-R
Xuan Loc basalts
Indian MORB

Figure 5.

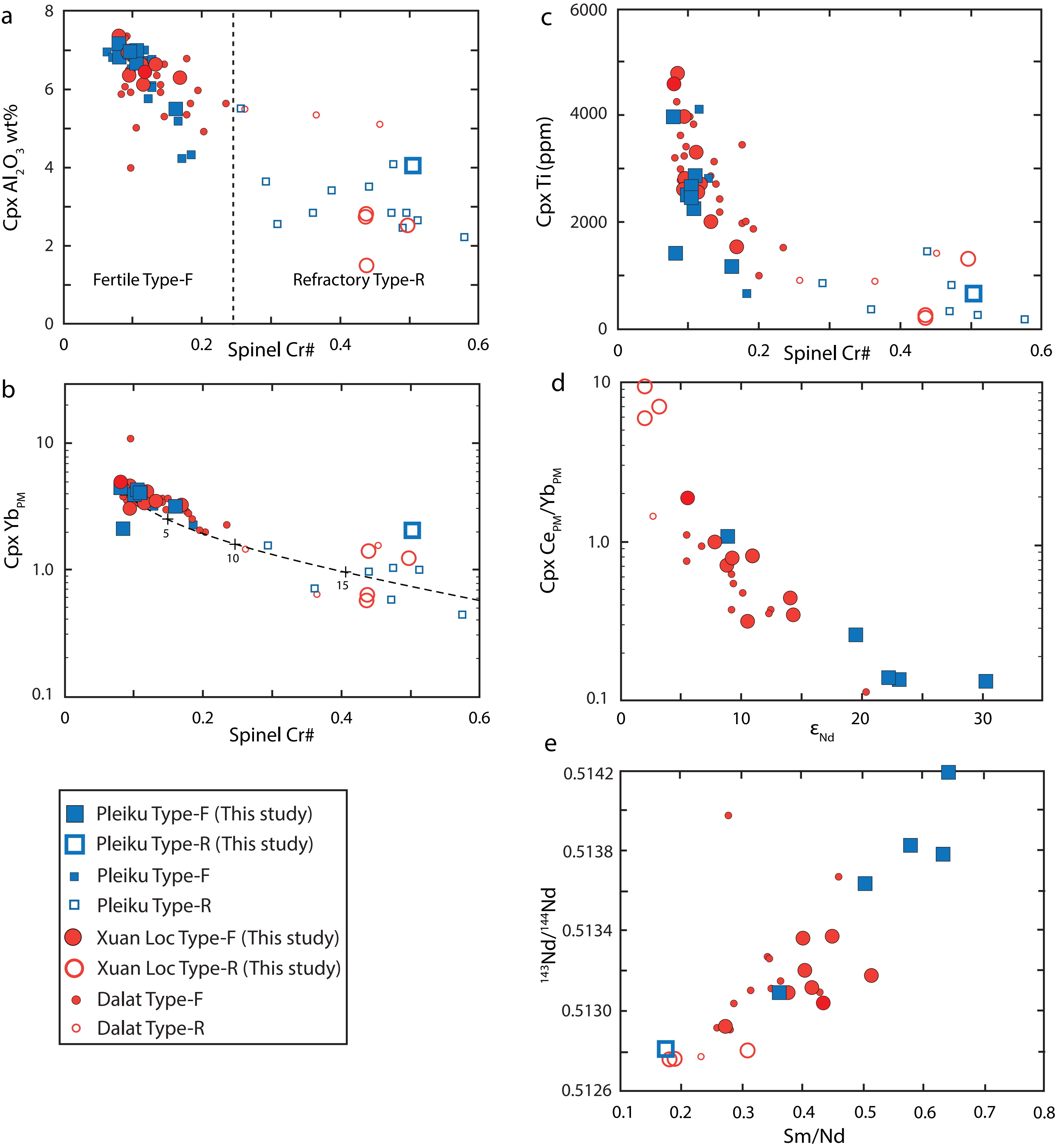
a
Cpx Al2O3 wt%
Fertile Type-F
Refractory Type-R
Spinel Cr#
b
Cpx YbPM
5
10
15
Spinel Cr#
c
Cpx Ti (ppm)
Spinel Cr#
d
Cpx CePM/YbPM
εNd
e
143Nd/144Nd
Sm/Nd
Pleiku Type-F (This study)
Pleiku Type-R (This study)
Pleiku Type-F
Pleiku Type-R
Xuan Loc Type-F (This study)
Xuan Loc Type-R (This study)
Dalat Type-F
Dalat Type-R

Figure 6.

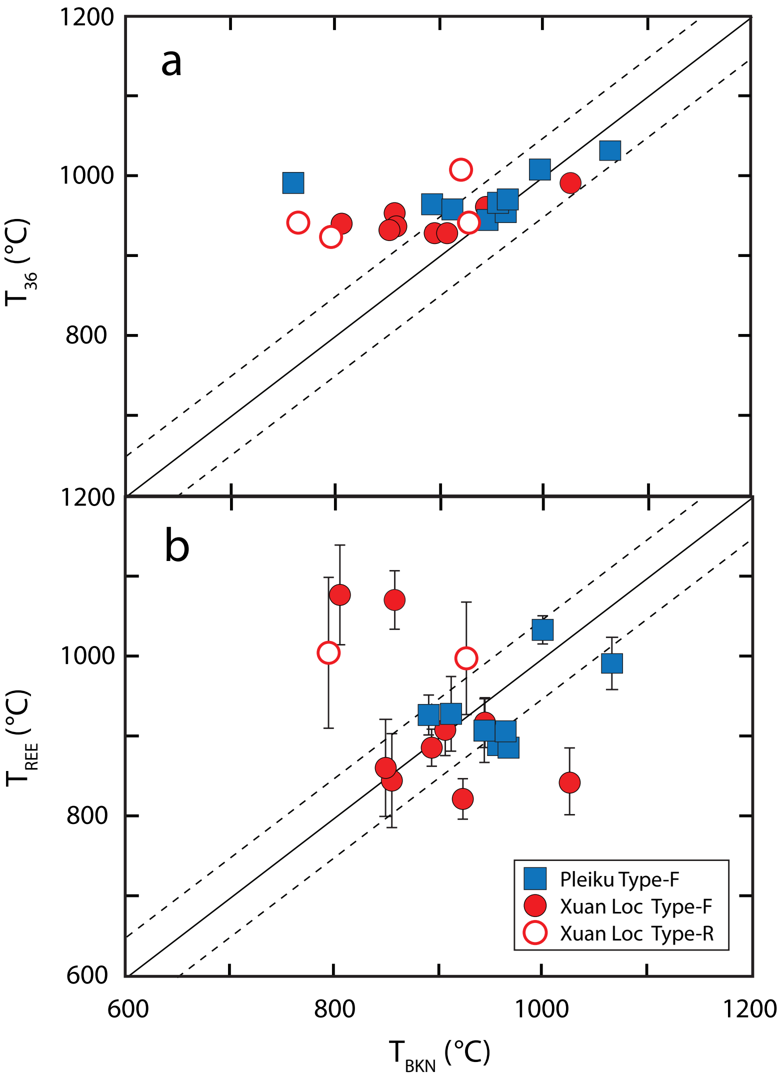

a
b
1200
1000
800
600
T36 (°C)
TREE (°C)
TBKN (°C)
Pleiku Type-F
Xuan Loc Type-F
Xuan Loc Type-R

Figure 7.

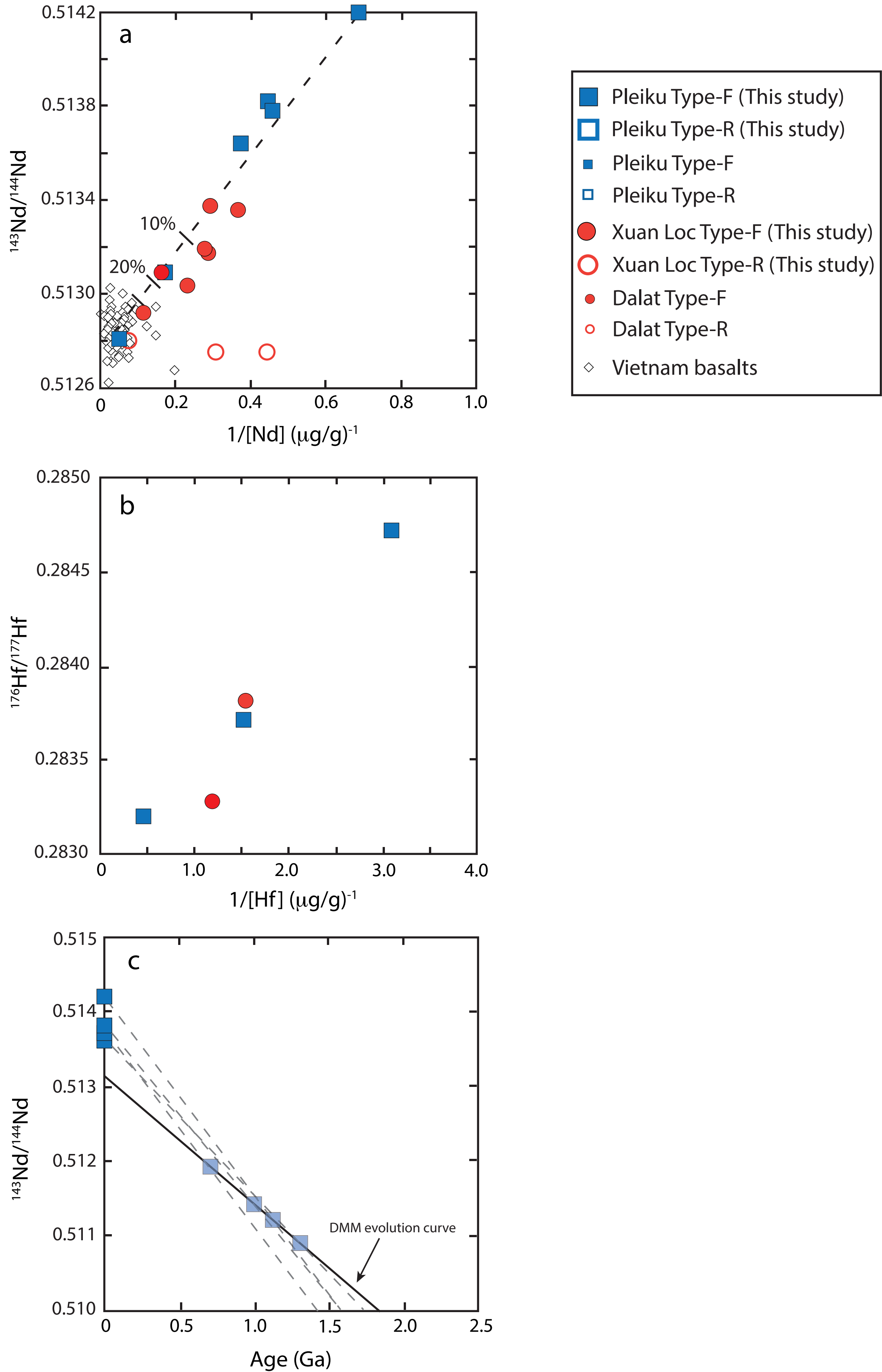

a
b
c
143Nd/144Nd
1/[Nd] (μg/g)-1
176Hf/177Hf
1/[Hf] (μg/g)-1
Age (Ga)
10%
20%
DMM evolution curve
Pleiku Type-F (This study)
Pleiku Type-R (This study)
Pleiku Type-F
Pleiku Type-R
Xuan Loc Type-F (This study)
Xuan Loc Type-R (This study)
Dalat Type-F
Dalat Type-R
Vietnam basalts

Figure 8.

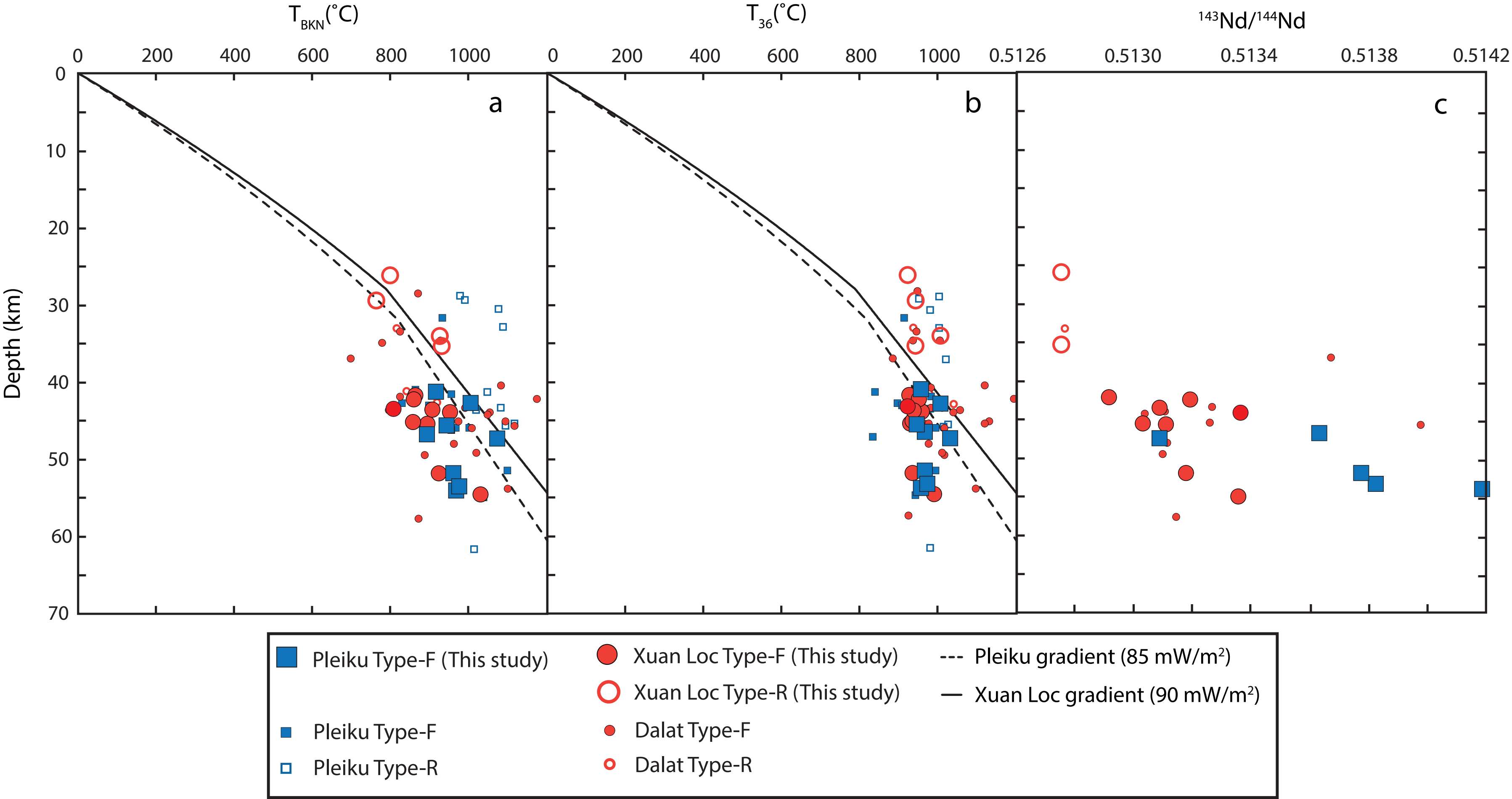

T$_{BKN}$(˚C)
T$_{36}$(˚C)
^{143}Nd/^{144}Nd
0
200
400
600
800
1000
0.5126
0.5130
0.5134
0.5138
0.5142
a
b
c
Depth (km)
0
10
20
30
40
50
60
70
Pleiku Type-F (This study)
Xuan Loc Type-F (This study)
Xuan Loc Type-R (This study)
Pleiku gradient (85 mW/m^2)
Xuan Loc gradient (90 mW/m^2)
Pleiku Type-F
Pleiku Type-R
Dalat Type-F
Dalat Type-R

Geochemistry, Geophysics, Geosystems

Supporting Information for

Characterizing Peridotite Xenoliths from Southern Vietnam: Insight into the Underlying Lithospheric Mantle

Kirby P Hobbs[1], Lynne J. Elkins[1], John C. Lassiter[2], Nguyen Hoang[3], Caroline M. Burberry[1]

[1] University of Nebraska-Lincoln, Lincoln, NE, USA

[2] Jackson School of Geoscience, University of Texas at Austin, Austin, TX, USA

[3] Institute of Geological Sciences, Vietnam Academy of Science and Technology (VAST), Hanoi, Vietnam

Contents of this file

Figures S1 to S3

Additional Supporting Information (Files uploaded separately)

Captions for Tables S1 to S2

Introduction

This supplement includes major and trace element data tables for samples from this study, and supporting figures showing representative xenolith mineral separates and rare earth element equilibration temperature calculations for each sample considered.

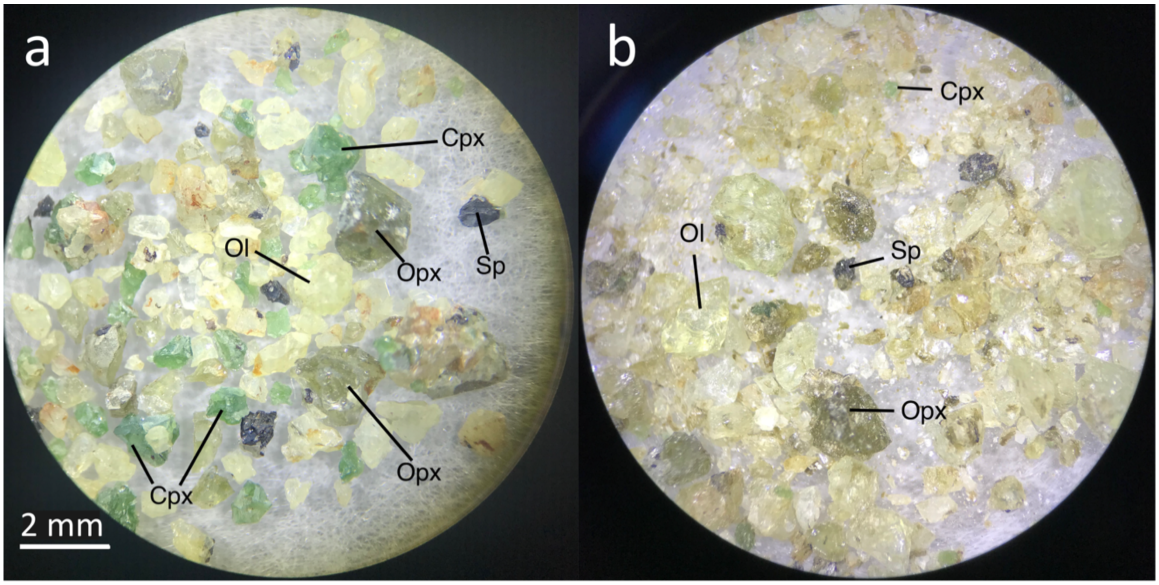

Figure S1. Olivine (Ol), orthopyroxene (Opx) clinopyroxene (Cpx), and spinel (Sp) mineral separates of **a)** a fertile sample (VN-2018-21-PL-2) and **b)** a refractory sample (VN-2018-36-XL-12). Fertile samples have higher modal cpx and, therefore, have higher potential to generate melting. Refractory samples have lower modal cpx, likely due to previous melt extraction.

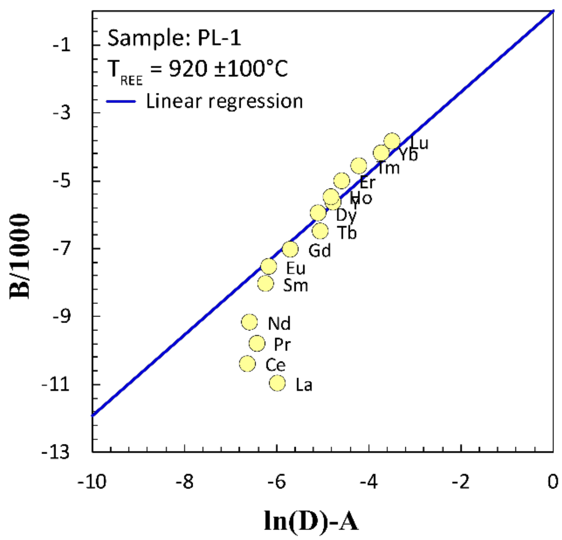
Sample: PL-1
T_REE = 920 ±100°C
Linear regression
B/1000
ln(D)-A
La Ce Pr Nd Sm Eu Gd Tb Dy Y Ho Er Tm Yb Lu

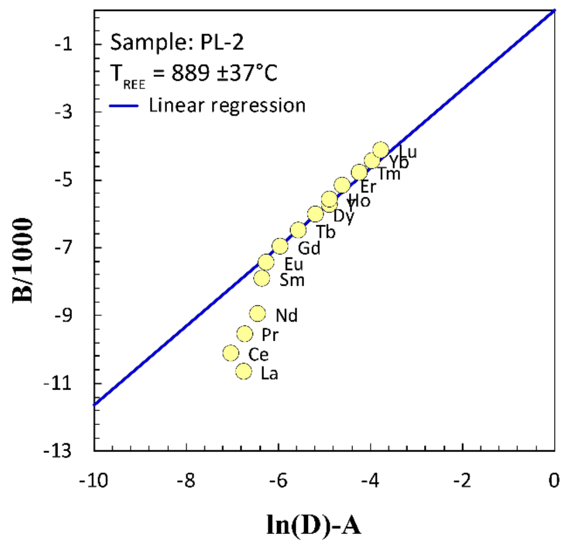
Sample: PL-2
T_REE = 889 ±37°C
Linear regression
B/1000
ln(D)-A
La Ce Pr Nd Sm Eu Gd Tb Dy Y Ho Er Tm Yb Lu

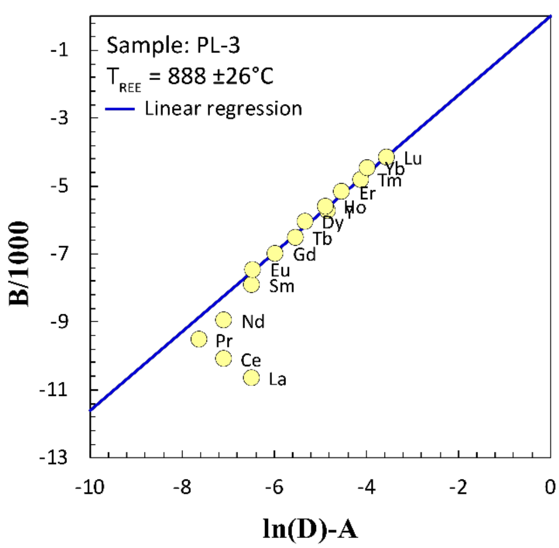
Sample: PL-3
T_REE = 888 ±26°C
Linear regression
B/1000
ln(D)-A
La Ce Pr Nd Sm Eu Gd Tb Dy Y Ho Er Tm Yb Lu

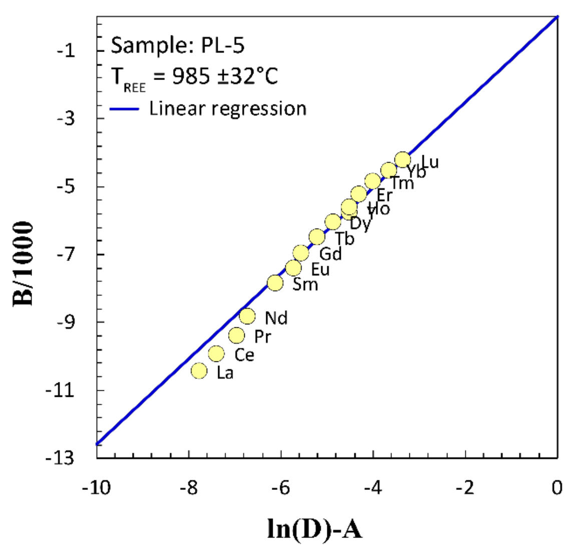
Sample: PL-5
T_REE = 985 ±32°C
Linear regression
B/1000
ln(D)-A
La Ce Pr Nd Sm Eu Gd Tb Dy Y Ho Er Tm Yb Lu

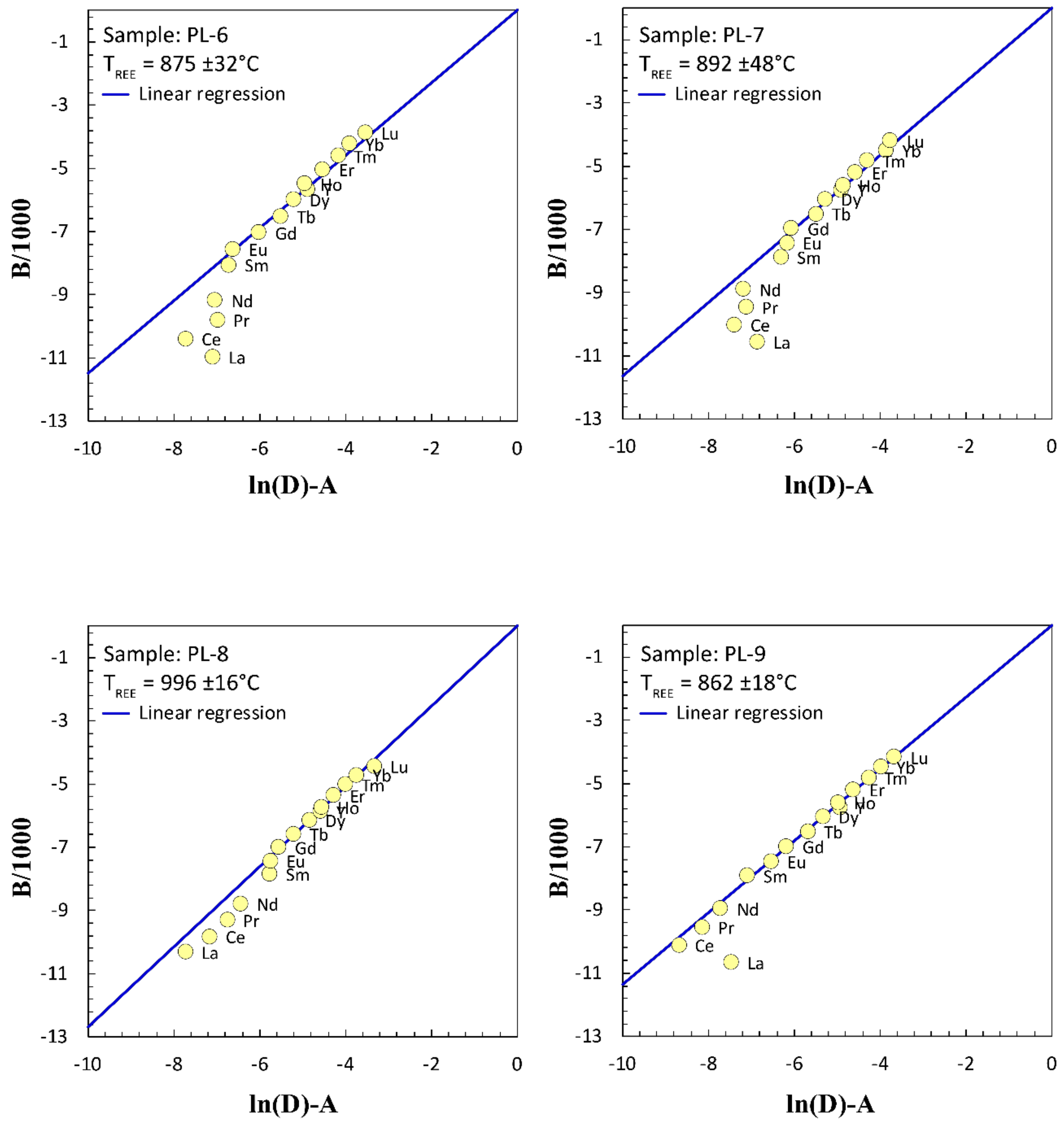
Sample: PL-6
T_REE = 875 ±32°C
Linear regression
Lu
Yb
Tm
Er
Ho
Dy
Tb
Gd
Eu
Sm
Nd
Pr
Ce
La
B/1000
ln(D)-A
Sample: PL-7
T_REE = 892 ±48°C
Linear regression
Sample: PL-8
T_REE = 996 ±16°C
Linear regression
Sample: PL-9
T_REE = 862 ±18°C
Linear regression

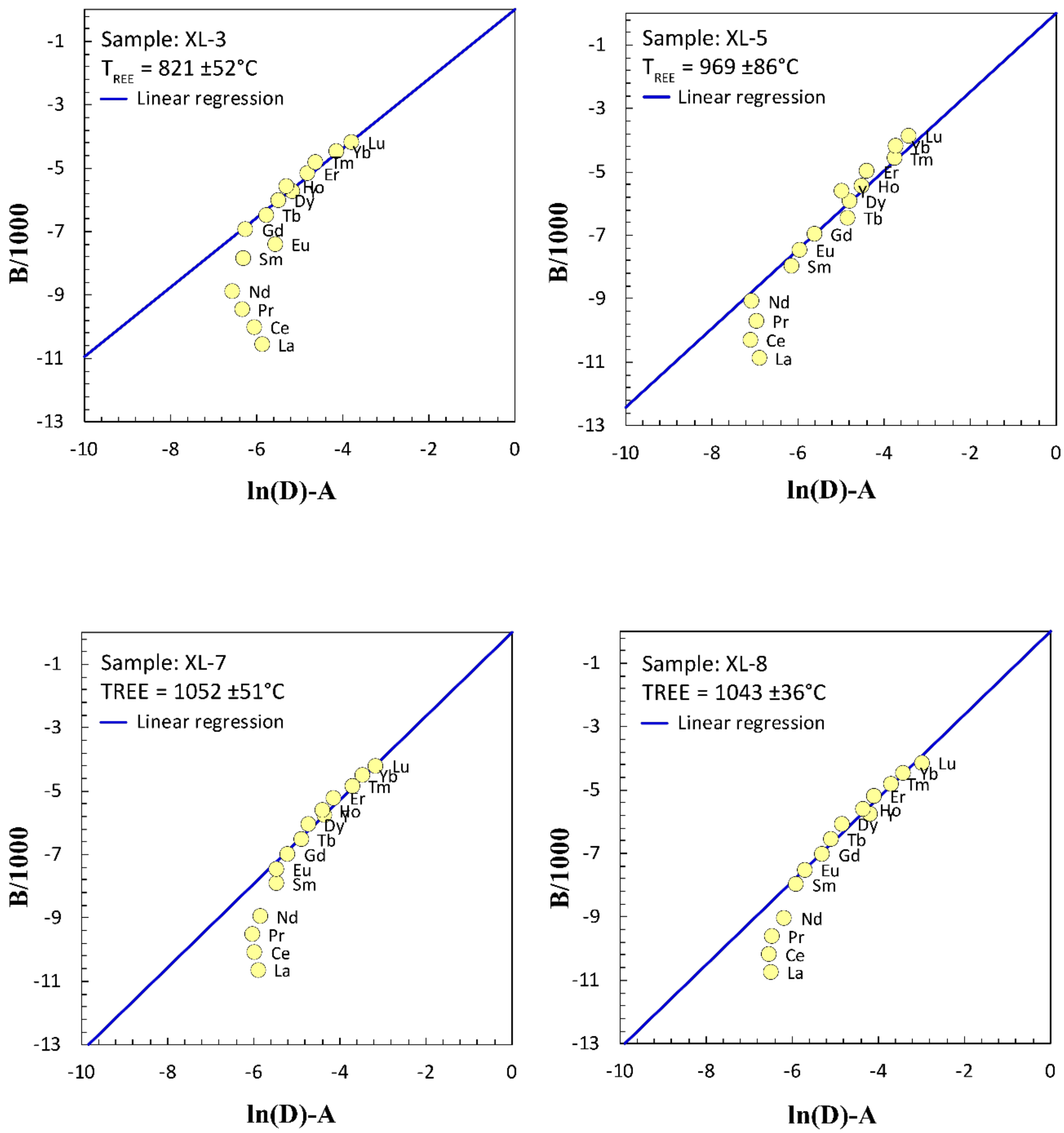
Sample: XL-3
T REE = 821 ±52°C
Linear regression
Sample: XL-5
T REE = 969 ±86°C
Linear regression
Sample: XL-7
TREE = 1052 ±51°C
Linear regression
Sample: XL-8
TREE = 1043 ±36°C
Linear regression
B/1000
ln(D)-A
La Ce Pr Nd Sm Eu Gd Tb Dy Y Ho Er Tm Yb Lu

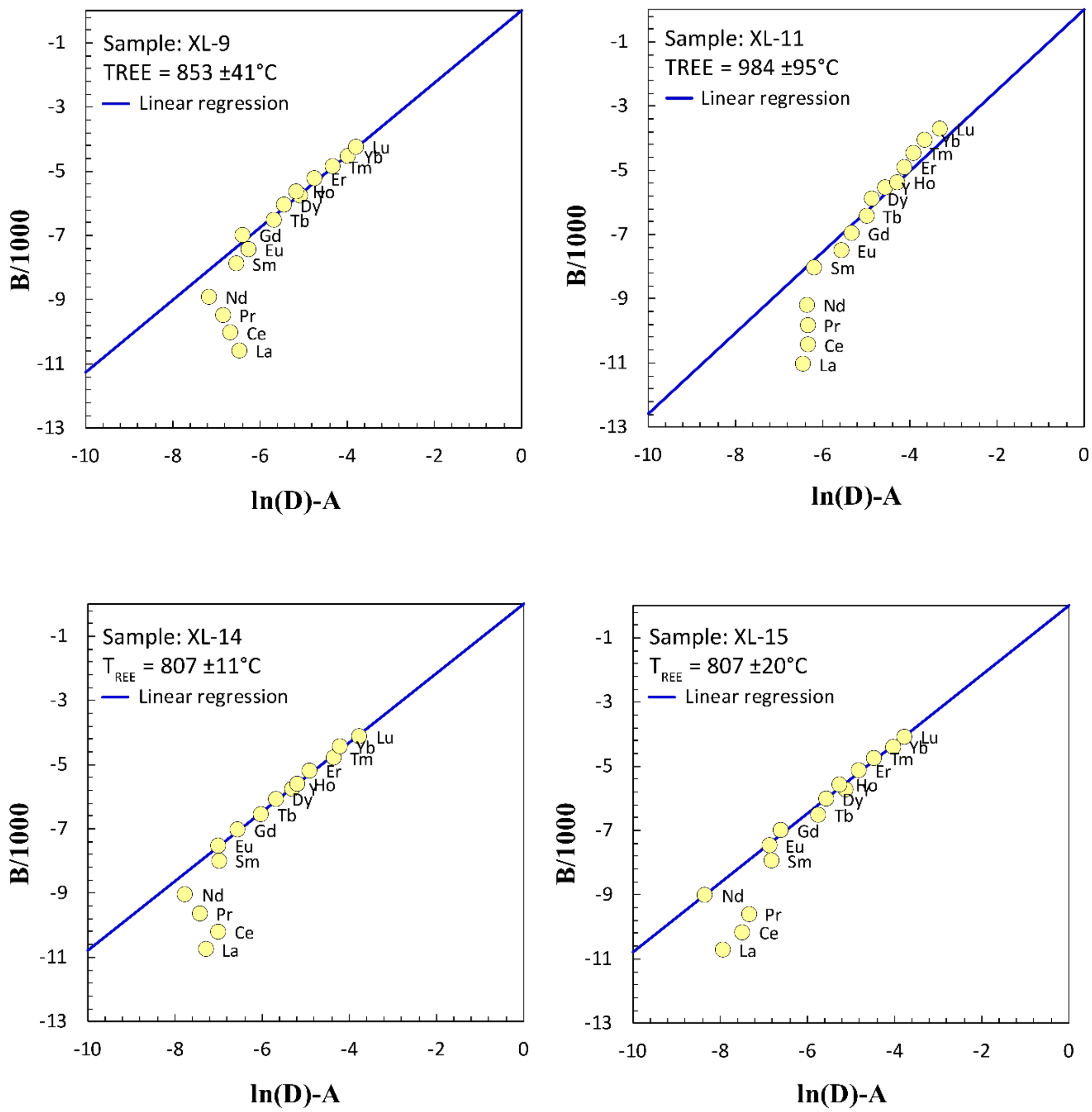
Sample: XL-9
TREE = 853 ±41°C
Linear regression
B/1000
ln(D)-A
La
Ce
Pr
Nd
Sm
Eu
Gd
Tb
Dy
Ho
Er
Tm
Yb
Lu
Sample: XL-11
TREE = 984 ±95°C
Linear regression
B/1000
ln(D)-A
Sample: XL-14
T_{REE} = 807 ±11°C
Linear regression
B/1000
ln(D)-A
Sample: XL-15
T_{REE} = 807 ±20°C
Linear regression
B/1000
ln(D)-A

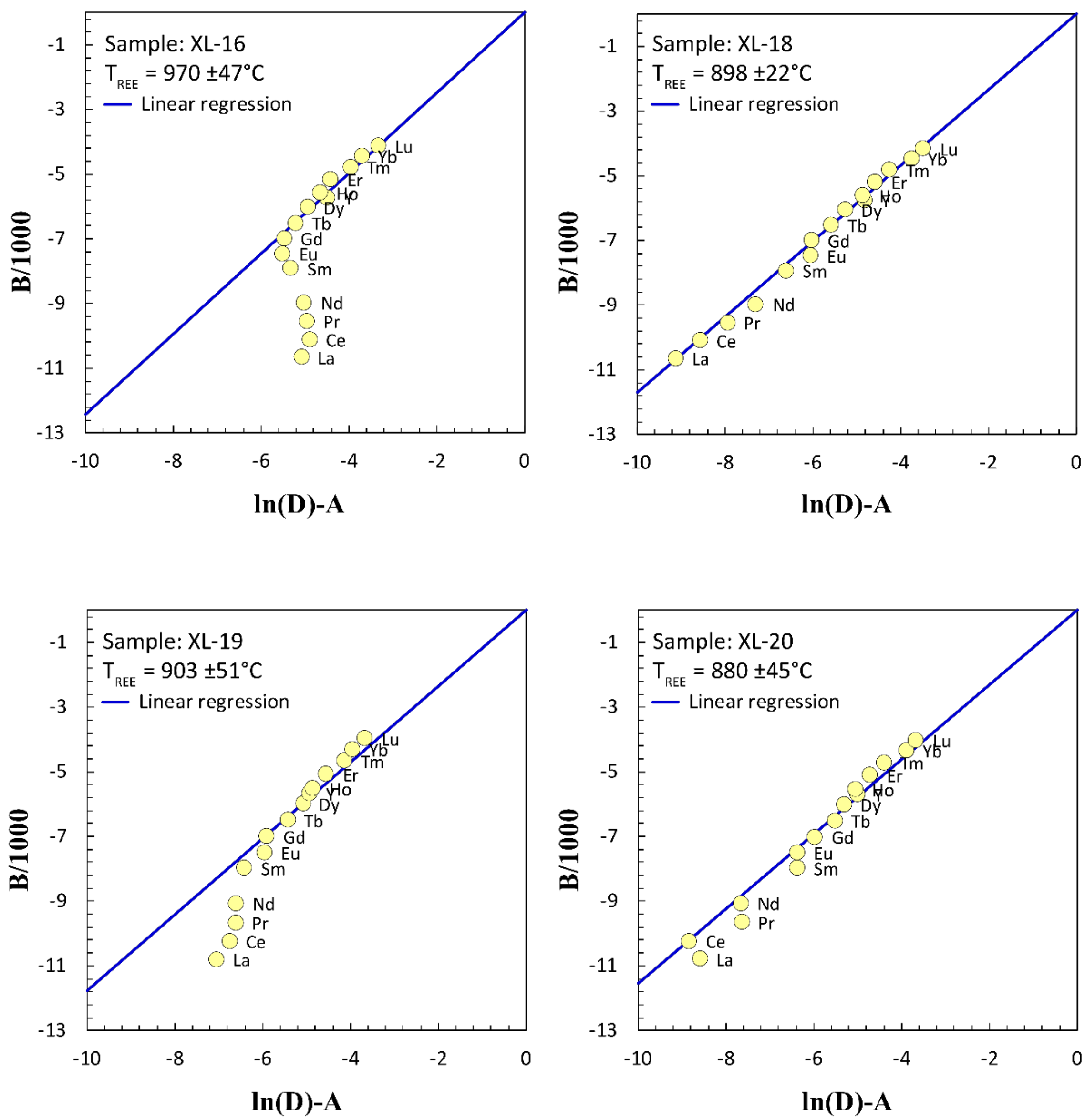

Figure S2. T_{REE} inversion diagrams for individual Vietnam xenolith clinopyroxene measurements from this study, for each xenolith sample as marked. Diagrams are shown for methods after Liang et al. (2013).

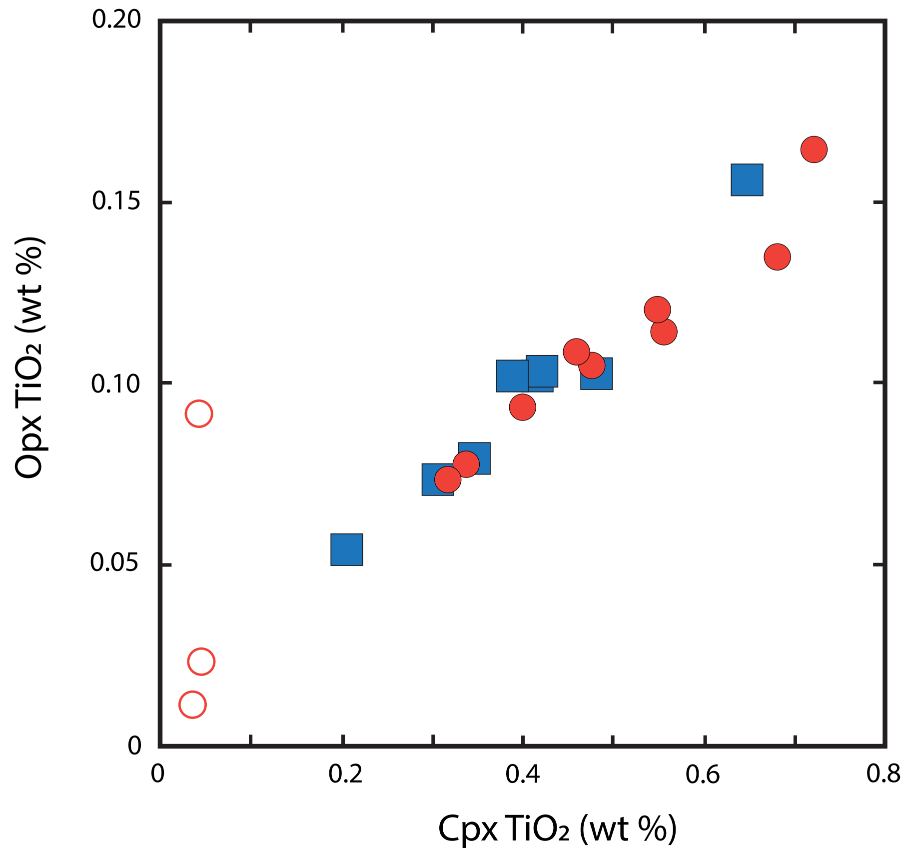

Figure S3. Orthopyroxene vs. clinopyroxene TiO2 contents in samples from this study. Overall, samples lie along a strong positive correlation, indicating that pyroxenes in these samples are largely in chemical equilibrium for thermobarometry purposes.

Table S1. (See separate supplementary file.) Average major element compositions of core and rim measurements for minerals from Vietnam xenoliths. Uncertainties are expressed as 1σ standard deviation.

Table S2. (See separate supplementary file.) Average trace element compositions (ppm) of clinopyroxene (cpx) and orthopyroxene (opx) in Vietnam xenoliths. Uncertainties expressed as 1σ standard deviation.

Supplementary References

Liang, Y., Sun, C., & Yao, L. (2013). A REE-in-two-pyroxene thermometer for mafic and ultramafic rocks. *Geochimica et Cosmochimica Acta* **102**, 246–260, doi:10.1016/j.gca.2012.10.035.